Arab American University

Faculty of Graduate Studies

Enhanced Conducting SiO_2 Nanosheets Designed as Transparent Optical Windows

By

Zakia Bilal Mahmoud Abu Abied

Supervisor

Prof. Dr. Atef Fayez Qasrawi

This thesis was submitted in partial fulfillment of the requirements for the Master's degree in Physics

July/2024.

Thesis Approval

Enhanced conducting SiO2 nanosheets designed as transparent optical windows.

By

Zakia Bilal Mahmoud Abu Abied

This thesis was defended successfully on 9/7/2024 and approved by:

Committee members	Signature
1. Prof. Dr. Atef Fayez Qasrawi: Supervisor	…………………
2. Prof. Dr. Hazem Khanfar: Internal Examiner	…………………
3. Prof. Dr. Mohammd El-Said: External Examiner	M.Khalil

Declaration

The work provided in this thesis, unless otherwise referenced, is the researcher's own work and has not been submitted elsewhere for any other degree or qualification.

The Name of The Student: Zakia Bilal Abu Abied

ID: 202120207

Signature: Zakia AbuAbied

Date: 19/12/2024

Acknowledgment

Praise be to God, who made beginnings easy and enabled us to reach the end.

I dedicate this success first to my ambitious self, which started with ambition and ended with success, and then to everyone who helped me complete my university journey.

To that great man who always encouraged me to reach my ambitions, to the one who awaited these moments to be proud of me….my dear grandfather.

To the one whose name I carry with pride and honor, to the one who lit my path and taught me that life is a struggle and its weapon is knowledge and learning, to my father.

To the unseen hand that removed thorns from my path, to the one who endured every moment of pain I went through, supported me, and stayed up long nights for my comfort, to the tender heart... to my beloved mother.

To those who supported me with love during my times of weakness and cleared all obstacles from my path, paving the way for me, planting confidence and determination within me...my support and the shoulder I always lean on... to my brothers.

To those who supported me with love and guidance, always provided me with strength, and were my refuge in all my hardships, whom God blessed me with to know the taste of life through them... to lifelong friends.

To Dr. Professor Atef Qasrawi, who left a beautiful mark with his ethics and cooperation, to the one who taught me morals before letters...I ask God for all the success for him.

Abstract

In this thesis, transparent conducting substrates suitable for optoelectronic devices have been fabricated. The conducting substrate is made of two stacked layers of SiO_2 sandwiched with Au nanosheets of thicknesses of 50 nm, 100 nm, and 200 nm to form SiO_2 / Au / SiO_2 (SAS-xx) trilayers. SAS substrates are subjected to structural and optical analysis to explore the possible physical modifications that resulted from the participants of the Au layer in the structure of SiO_2. It is observed that Au nanosheets didn't alter the amorphous nature of the structure of SiO_2 but enhanced its optical properties significantly. Particularly, it is observed that SAS-00 samples not comprising Au exhibit high transmittance and low reflectance. The thicker the Au layer, the lower the transmittance and the higher the reflectance. Thicker layers of Au also resulted in a decrease in the light absorption of SiO_2. However, Au nanosheet enhanced the free carrier absorption in the infrared range of light and decreased the energy band gap of SiO_2. SAS samples comprising no Au, Au nanosheet of a thickness of 50 nm exhibited non-degenerate semiconductor characteristics and showed the presence of energy tail states in the band gap. The tail states disappeared as the Au thickness was increased further. It is also observed that the Au nanosheet improves the dielectric constant value and dispersion. SAS-200 samples showed a high k-gate dielectric material feature with a relative dielectric constant value exceeding 40. In addition, it is observed that the Au nanosheet increased the optical conductivity and the free charge density in SiO_2 films, making them highly conductive and semitransparent. Substrates with these characteristics are promising for use as high-k-gate electrodes and for the design of optoelectronic devices.

Table of Contents

List of Tables

List of Figures

List of Definitions of Abbreviations

Symbol	**Symbol abbreviation**
SAS-00	Silicon Oxide - Gold - Silicon Oxide with coating no gold nanosheet
SAS-50	Silicon Oxide -Gold -Silicon Oxide comprising a 50nm thickness of Gold
SAS-100	Silicon Oxide - Gold - Silicon Oxide comprising a 100 nm thickness of Gold
SAS-200	Silicon Oxide - Gold - Silicon Oxide comprising a 200 nm thickness of Gold
λ	Wavelength
d	Inter-planer distance
θ	Bragg angle
n	Integer
E_g	Energy band gap
α	Absorption coefficient
T	Transmittance
R	Reflectance
E_o	The width of the band tails

$\vec{E}$	The electric field
$\vec{H}$	The magnetic field
$\vec{J}$	The current density
$\vec{D}$	The electric field in the medium
$\vec{B}$	The magnetic field in the medium
ε	The complex dielectric function
μ	The complex magnetic permeability
σ	The complex electrical conductivity
$\vec{K}$	The complex propagation constant
w	The light frequency
ε_r	The real part of the dielectric constant
ε_{img}	The imaginary part of the dielectric constant
ε_{eff}	The effective dielectric constant
$\tilde{n}$	The real part of the complex refractive index

$\tilde{k}$	The imaginary part of the complex refractive index
m_o	The electron mass
ω	The angular frequency

Chapter One

Introduction

Nowadays, to fulfill the demands of the newest generations of optoelectronic devices with variable functionality, it requires significant efforts to work on existing traditional transparent conductors. These conductors should be developed into new material systems that are both electrically conductive and transparent. The transparent conductive films are irreplaceable components that are used in most optoelectronic applications like sensors, organic light-emitting diodes, solar cells, smartphones, and smart windows [1]. Some of the transparent conducting windows, including titanium dioxide (TiO_2) [2], tin-doped indium oxide (ITO), fluorine-doped tin oxide (FTO), and silicon dioxide (SiO_2), are regarded as oxide semiconductors, which are significant and highly useful as transparent conducting window layer materials. These semiconducting materials find applications in fiber- based solar cells [3], light-emitting devices, anti-reflection coatings in nanoscale electronics [4], etc.

Among those, SiO_2 has poor electrical but good optical, and chemical properties, such as high transmittance that is greater than 92% in the infrared range (800–1200 nm). [5], low absorption , high corrosion resistance, high thermal stability, amorphous structure [6], a wide optical band gap, which is 8.90 eV, a highly transparent insulator [7], and nanostructures with diverse applications. Silicon dioxide in nanosheet forms [8] is taken into consideration for this study.

SiO_2 thin film can be deposited by various methods, including the sol-gel method [9] [10] [11], chemical vapor deposition [12], atomic layer deposition (ALD) [13] [14] [15], plasma ion assisted deposition method [16] [17], sputtering [18], plasma-enhanced chemical vapor deposition (PECVD) [19] [20], and electron beam (e-beam) evaporation [21]. Moreover, the SiO_2 transparent conductive windows provide great performance, a distinct structure, and several application possibilities.

In this study, we aim to construct a transparent conductive window by stacking layers of SiO_2 nanosheets as optical windows. The stacked silicon dioxide layers are sandwiched with metal nanosheets of various thicknesses. The work here will always focus on the changes in optical transmittance, reflectance. Enhanced optical properties are expected to result from metal sandwiching. Those windows will be brought to a stage that makes it preferable for most semiconductors to work as a conducting transparent electrodes. Various techniques, including ion coating, X-ray diffraction, scanning electron microscopy, optical spectroscopy, and hot probe techniques, will be employed to characterize the devices.

In the second chapter of this thesis, we will be discussed theoretical background of the basics mathematics used to analyses the result. Details and procedures for the experiments will be discussed in chapter three. Chapter four shows the achieved results, explanations, and discusses the observations. Finally, chapter five will contain concluding remarks on our work.

Chapter Two

Theoretical Background

2.1 Crystalline nature

Crystal structure refers to the spatial arrangement of ions, atoms, and molecules. It is a distinct arrangement of atoms in a crystal. It is a critical component of materials science and engineering since many of the characteristics of materials are determined by their crystal structure. The amorphous structure is a random arrangement of atoms. It have a significant advantage over crystals in that they have a substantially smaller band gap than their crystalline counterparts, allowing them to provide a wider light absorption spectrum. [22]

2.2 The X-ray diffraction:

The X-ray scattering method reveals details on the crystal structure and structural properties of materials and thin films. The properties of materials are determined by their crystal structures; hence, x-ray diffraction methods are extensively employed as an essential tool in material research and development. Basically, Fig. 2.1 shows an XRD device that consists of the X-ray source, a sample stage, and the X-ray detector. Also in this figure, the angle θ is located between the plane of the sample and the X-ray source, while the angle 2θ is the angle between the X-ray source and the detector. Each atom in the sample scattered the incident monochromatic X-ray beam.

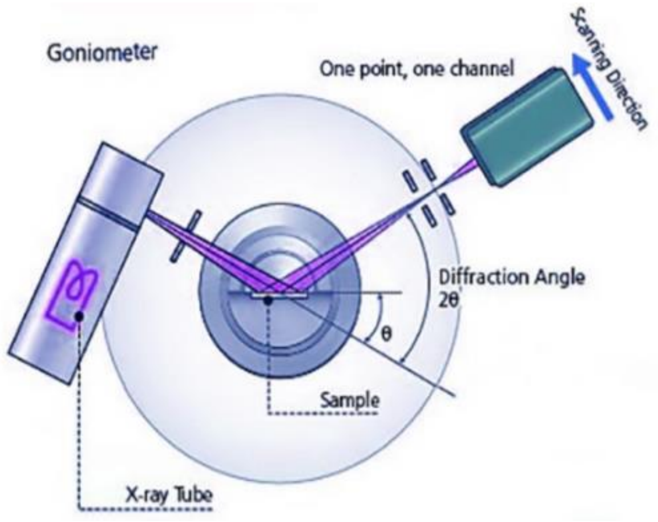

Fig. 2.1: The schematic diagram of the X-ray diffractometer. [23]

Here, the constructive interference occurs if the scattered beams are in phase and the crystalline nature of the material appears; otherwise, the destructive interference occurs and the amorphous nature of the material appears. The interplanar distance between two planes of the material atom can be defined with the help of Bragg's law.

2.2.1 Bragg's Law:

Bragg's law under constructive interference appears when the angle diffraction (θ), the wavelength of the reflected X-ray, and the interplanar distance between the atomic planes (d) are as the Fig. 2.2 shows.

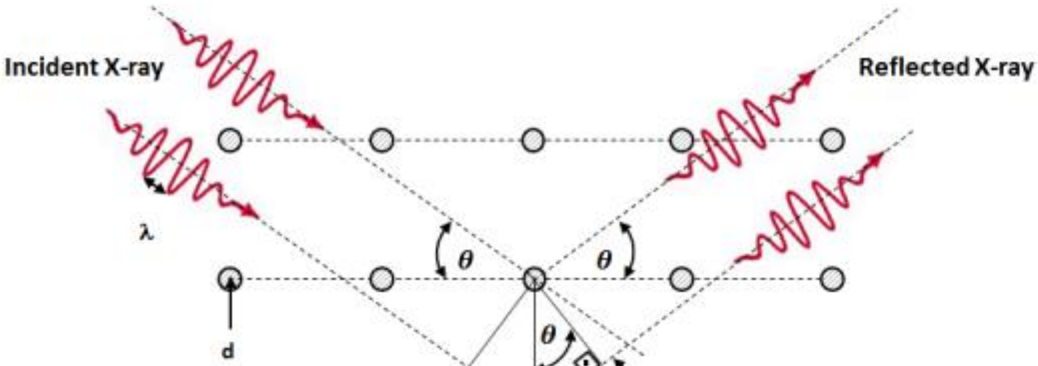

The constructive interference occurs only when:

$$n\lambda = AB + BC \tag{2.1}$$

But as : AB=BC, so:

$$n\lambda = 2AB \tag{2.2}$$

$$\sin\theta = AB/\, d \tag{2.3}$$

$$AB = d\,\sin\theta \tag{2.4}$$

Inserting into equation (2.2), which give Bragg's law [24]:

$$2d\sin\theta = n\,\lambda \tag{2.5}$$

In this equation, d is the interplanar distance between two successive atomic planes, θ is the angle between the incident beam and the plane surface, n is a positive integer, and λ is the X-ray wavelength, which is equal to 1.5405 A°.

2.3 Optical properties in semiconductors

The optical properties of semiconductors play an important role in thin film development. It is the basis of the technological revolution.

2.3.1 Optical process characterization

The incident beam can then be transmitted or reflected outside the medium, and it can also be propagated inside it as illustrate in Fig.2.3. The four processes involved in linear optical propagation are refraction, absorption, luminescence, and scattering. Absorption is essentially influenced by the propagation of light frequencies. When the light frequency equals the frequency of solid material oscillation, the light is absorbed.[25]

Studies of optical properties include transmittance (T), reflectance (R), absorption coefficient (a), energy band gap (E_g), and dielectric constant (ε).

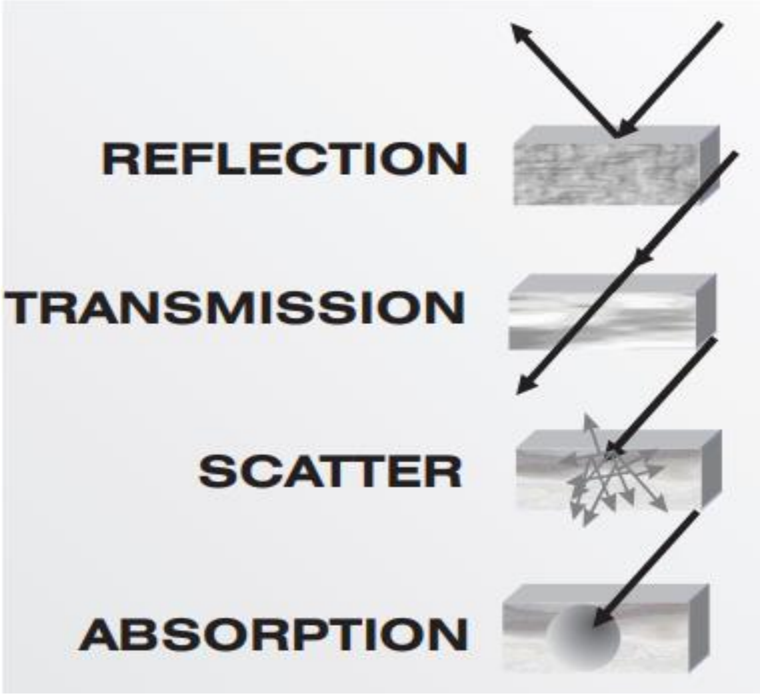

Fig. 2.3: Light reflectance, transmittance, scatter and absorbance.[26]

2.3.2 Absorption of light in matter.

If the photon is absorbed inside the material, it provides electrons with kinetic energy, freeing them. During the absorption process, electrons are transferred from the valence band to the conduction band. The material's light absorption is defined by the absorption coefficient (α), which represents the rate of incoming light intensity attenuation over the propagation distance. Transmittance refers to the efficiency with which radiant energy passes through a volume. The light transmittance in a thick optical material with thickness l may be expressed as [27]:

$$T = (1 - R_1)(1 - R_2)e^{-\alpha l} \tag{2.6}$$

Where R_1 and R_2 are the reflectivities of the front and back surfaces, respectively. Also, the terms $(1 - R_1)\ and (1 - R_2)$ are they reflect the transmittance of the front and back surfaces, respectively. While the expression describes the exponential decrease in light intensity with distance [28]. In addition, when two materials are placed on the glass substrate, the transmittance is:

$$T = (1 - R_1)(1 - R_2)(1 - R_3)e^{-\alpha l} \tag{2.7}$$

Thus, the absorption coefficient α at thickness l=d is written as:

$$\alpha = \frac{1}{d}\ln\left(\frac{T}{(1-R_1)(1-R_2)(1-R_3)}\right) \tag{2.8}$$

Similarly, the absorption coefficient α for four materials placed on a glass substrate is given by:

$$\alpha = \frac{1}{d}\ln\left(\frac{T}{(1-R_1)(1-R_2)(1-R_3)(1-R_4)}\right) \tag{2.9}$$

In this work, R_1, R_2, R_3, and R_4 represent the reflectance of glass, SiO_2 , SiO_2,/Au, and SiO_2,/Au/ SiO_2, respectively. And d is the thickness of the thin film layer.

2.3.3 Tauc's equation and band gap calculations

Electrons in an isolated atom have different energy levels, but when atoms are brought together, the degenerate energy levels divide into multiple levels as a result of atomic interaction; the levels may be viewed as a continuous band of allowed energy states since they are so close together. The highest energy bands are the valence and conduction bands. The valance and conduction bands are separated by a region that represents energy that electrons in the material cannot possess due to quantum selection values; this region is called the band gap (E_g) [29].The optical band gap of semiconductors is calculated using Tauc's equation and absorption coefficient spectra. According to Tauc's equation, the energy band gap is exactly proportional to $(\alpha E)^{P}$. The exponent (p) indicates the type (characteristic) of the transition. The formula for Tauc's equation is [30]:

$$(\alpha E)^{\frac{1}{p}} = B(E - E_g) \tag{2.10}$$

Where $E = h\nu$ is the incident photon energy and p is an index that describes the optical absorption process, it can have values of 1/2, 2, 3/2, and 3 for direct allowed, indirect allowed, direct forbidden, and indirect forbidden electronic transition between valence and conduction bands, respectively. B is a constant that depends on the electron transition probability, and E_g is the energy band gap between valance band and conduction band.

We began by using the energy band diagram shown in Fig. 2.4 to derive this equation.

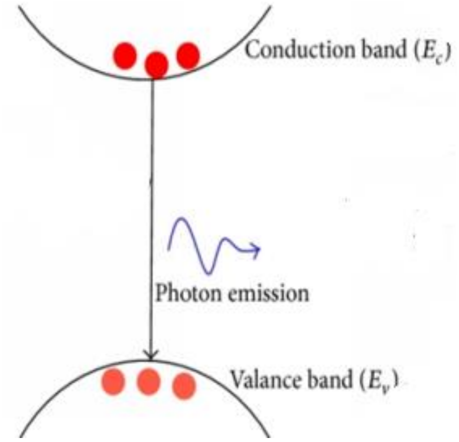

Fig. 2.4: The energy band gap diagram. [31]

From Fig.2.4 the final energy equal to:

$$E_f = hv - E_i \qquad (2.11)$$

The initial and final energy states of the bands are also given by [32]:

$$E_f - E_g = \frac{\hbar^2 k^2}{2m_e^*} \qquad (2.12)$$

And,

$$E_i = \frac{\hbar^2 k^2}{2m_e^*} \qquad (2.13)$$

When incoming photons interact with solids, the electrons travel from the valence band up to the conduction band, where:

$$E_f = hv - |E_i| \qquad (2.14)$$

Subtract E_g from both sides of equation (2.14) to get:

$$E_f - E_g = hv - E_g - |E_i| \qquad (2.15)$$

Substitute equation (2.12) & (2.13) in equation (2.15) to give:

$$\frac{ħ^2k^2}{2m_e^*} = hv - E_g - \frac{ħ^2k^2}{2m_h^*} \tag{2.16}$$

Rewrite equation (2.16) in the form:

$$hv - E_g = \frac{ħ^2k^2}{2m_e^*} + \frac{ħ^2k^2}{2m_h^*} = \frac{ħ^2k^2}{2}[\left(\frac{1}{m_e^*}\right) + \left(\frac{1}{m_h^*}\right)] \tag{2.17}$$

The state density in an energy range extended from (hv) to (hv+$d(hv)$) have the form [32]:

$$N(hv)d(hv) = \frac{8\pi k^2 dk}{(2\pi)^3} \tag{2.18}$$

Rewrite equation (2.17) to give:

$$k^2 = \frac{2(hv - E_g)}{ħ^2} m_r \tag{2.19}$$

m_r is the reduce mass, where:

$$\frac{1}{m_r} = \left(\frac{1}{m_e^*}\right) + \left(\frac{1}{m_h^*}\right) \tag{2.20}$$

Deriving equation (2.19) with respected to (hv), where k is a functional of hv to get :

$$kdk = \frac{m_r}{ħ^2} d(hv) \tag{2.21}$$

Substitute equation (2.19) in equation (2.18) to give:

$$N(hv)d(hv) = \frac{16\pi(hv - E_g)m_r}{ħ^2(2\pi)^3} dk \tag{2.22}$$

By employing equation (2.19) in equation (2.21) in the previous equation (2.22) the state density equation will be:

$$N(hv)d(hv) = \frac{16\pi\left(hv-E_g\right)}{\hbar^2(2\pi)^3}\frac{\mathrm{m_r^2}}{\hbar^2\left(\frac{\sqrt{(2\left(\mathrm{hv-E_g}\right)\mathrm{m_r}}}{\hbar^2}\right)}d(hv) \tag{2.23}$$

Rewriting equation (2.23) in another form:

$$N(hv)d(hv) = \frac{(2m_r)^{\left(\frac{3}{2}\right)}}{2\pi^2\hbar^3}\left(hv-E_g\right)^{\frac{1}{2}}d(hv) \tag{2.24}$$

The initial and final state densities, N_i and N_f, respectively, have a linear relationship with the absorption coefficient:

$$\alpha(hv) = B\left(hv-E_g\right)^{1/2} \tag{2.25}$$

Where

$$B = \frac{q^2\left(\frac{2m_h^* m_e^*}{m_h^*+m_e^*}\right)^{\frac{1}{2}}}{nch^2 m_e^*} \tag{2.26}$$

$$= \frac{q^2(m_r)^{\frac{1}{2}}}{nch^2 m_e^*} \tag{2.27}$$

To generalize equation (2.25) rewrite it to become:

$$(aE)^{1/p} = B\left(E-E_g\right) \tag{2.28}$$

To estimate the energy gap for semiconductor materials, $(\alpha E)^{\frac{1}{p}}$ plotted against incident photon energy E, where the intercept of the E-axis in the linear region of the absorption with the baseline represents the E_g value.

2.3.4 Direct and indirect transitions

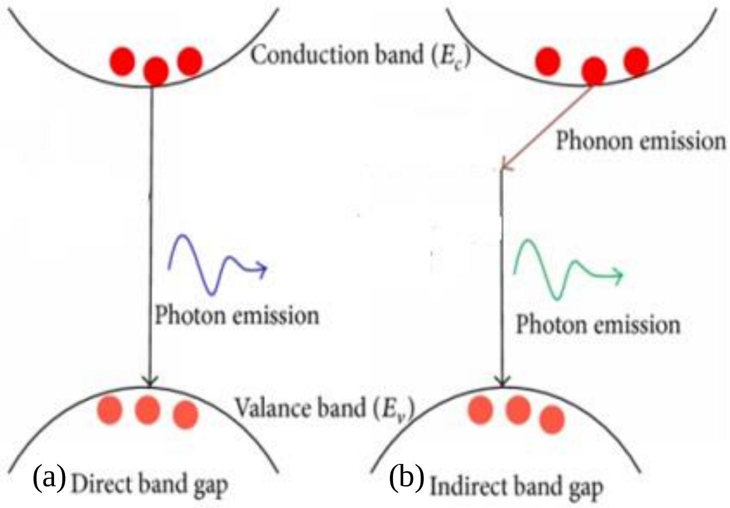

Fig. 2.5: The (a) direct and (b) indirect band gap transitions.[31]

A particular momentum (k-vector) in the Brillouin zone separates the maximal energy state in the valence band from the lowest energy state in the conduction band of semiconductors. The allowed direct absorption transition (Fig. 2.5 (a)) occurs when the valence band's top and conduction band's bottom have the same momentum [33]. The indirect band gap is created when the minimum energy of the conduction band and the maximum energy of the valence band occur at different k values [34]. The difference in k-vectors results in misalignment bands that require phonon help to absorb excited electrons into the conduction band. However, directly band gap materials don't require a change in crystal momentum (k), so no phonon assist is required [35]. In optoelectronics, solar energy conversion, and light emitting diodes (LEDs), direct band gap semiconductors are essential for several applications.[36]. On the other hand, indirect bandgap semiconductors are not effective light emitters because optical transitions over an indirect bandgap are forbidden.[37].

2.3.5 Energy Band Tails (E_e)

Along the absorption coefficient curve, if α displays a steady trend of variations when increasing the photon energy, this is called absorption saturation. In the low energy region, the presence of band tails is shown by a decreasing trend of variation with decreasing photon energy. While α shows an increasing trend of variation as photon energy decreases, this implies the presence of free carrier absorption.

The Urbach tail (E_e) is an exponential portion that depends on photon energy in the α – E spectra. Its rule is described as follows [38]:

$$\alpha = \alpha_0 \, e^{\frac{E}{E_e}} \tag{2.29}$$

In this equation, α represents the absorption coefficient, α_0 is a constant, E is photon energy, and E_e is the width of the band tail of the localized state associated with the amorphous state. Taking the logarithm of both sides of the equation (2.29), we get a straight line equation. It's given by:

$$\ln \alpha = \ln \alpha_0 + \frac{E}{E_e} \tag{2.30}$$

When ln (α) is plotted against incident photon energy (E), the slope of the straight-line used to calculate the entry band energies (E_e).

2.3.6 Dielectric spectra

The study of dielectric materials is particularly important in terms of refractive index dispersion. There is the complex dielectric constant and the complex optical conductivity, which are introduced through Maxwell's equations (assuming there is no charge density in the absence of incident light) as [39]:

$$\vec{\nabla} \times \vec{E} = -\frac{\partial \vec{B}}{\partial t} \tag{2.31}$$

$$\vec{\nabla} \times \vec{H} = \vec{J} + \frac{\partial \vec{D}}{\partial t} \tag{2.32}$$

$$\vec{\nabla}.\vec{D} = 0 \tag{2.33}$$

$$\vec{\nabla}.\vec{B} = 0 \tag{2.34}$$

Since $\vec{E}$ is the electric filed, $\vec{H}$ is the magnetic field, and $\vec{J}$ is the current density. While $\vec{D}$ and $\vec{B}$ are the electric and magnetic fields in the medium. To define the concepts of the complex dielectric function (ε), the complex magnetic permeability (μ), and the complex electrical conductivity (σ), the equations that are relating $\vec{D}, \vec{B}$, and $\vec{J}$ to the $\vec{E}$ and $\vec{H}$ fields can be expressed as:

$$\vec{D} = \varepsilon\vec{E} \tag{2.35}$$

$$\vec{B} = \mu \vec{H} \tag{2.36}$$

$$\vec{J} = \sigma \vec{E} \tag{2.37}$$

By taking the curl of equation (2.31) and substituting $\vec{B}$ and $\vec{\nabla} \times \vec{H}$ from equations (2.36) and (2.32), respectively. We get:

$$\vec{\nabla} \times \left(\vec{\nabla} \times \vec{E}\right) = -\mu \left(\frac{\partial \vec{J}}{\partial t} + \frac{\partial^2 \vec{D}}{\partial t^2}\right) \tag{2.38}$$

Then, substituting equations (2.37) and (2.35) into equation (2.38) to get:

$$\vec{\nabla} \times \left(\vec{\nabla} \times \vec{E}\right) = -\left(\mu\, \sigma \frac{\partial \vec{E}}{\partial t} + \mu\, \varepsilon \frac{\partial^2 \vec{E}}{\partial t^2}\right) \tag{2.39}$$

With the help of vector identity, the left-hand side of equation (2.39) can be simplified as:

$$\vec{\nabla} \times \left(\vec{\nabla} \times \vec{E}\right) = \vec{\nabla}\left(\vec{\nabla}.\vec{E}\right) - \vec{\nabla}^2 \vec{E} \tag{2.40}$$

Here, $\vec{\nabla}.\vec{E}$ is equal to zero if there is no charge density, and then the equation (2.40) becomes:

$$\vec{\nabla}^2 \vec{E} = \mu\, \sigma \frac{\partial \vec{E}}{\partial t} + \mu\, \varepsilon \frac{\partial^2 \vec{E}}{\partial t^2} \tag{2.41}$$

By taking the curl of equation (2.32) and eliminating $\vec{\nabla} \times \vec{J}$ and $\vec{\nabla} \times \vec{D}$ from equation (2.37) and (2.35), respectively. We get:

$$\vec{\nabla}^2 \vec{H} = \mu\, \sigma \frac{\partial \vec{H}}{\partial t} + \mu\, \varepsilon \frac{\partial^2 \vec{H}}{\partial t^2} \tag{2.42}$$

Equations (2.41) and (2.42) have sinusoidal solutions in the form

$$\vec{E} = E_0\, e^{i\left(\vec{K}.\vec{r} - \omega t\right)} \tag{2.43}$$

$$\vec{H} = H_0\, e^{i\left(\vec{K}.\vec{r} - \omega t\right)} \tag{2.44}$$

Where ω is the frequency of the light and K is the complex propagation constant. The real part of the complex propagation constant can be characterized as a wave vector, while the imaginary part indicates the wave's attenuation inside the material and corresponds to energy dissipation.

If we substitute the sinusoidal solution (2.43) into equation (2.41), then we get:

$$K^2 = \mu\varepsilon\omega^2 + i\mu\varepsilon\sigma \tag{2.45}$$

If there are no energy losses, K would be a real number and characterized as a wave vector as:

$$K_0 = \omega\sqrt{\mu\varepsilon} \tag{2.46}$$

If there are energy losses in the conducting medium, K will be a complex quantity defined as:

$$K = \omega\sqrt{\mu\varepsilon_{complex}} \tag{2.47}$$

Since the complex dielectric function can be defined as:

$$\varepsilon_{complex} = \varepsilon + \frac{i\sigma}{\omega} = \frac{i}{\omega}\left[\sigma + \frac{\varepsilon\omega}{i}\right] = \varepsilon_r + i\ \varepsilon_{img} \tag{2.48}$$

Since $\varepsilon_r\ and\ \varepsilon_{img}$ are both the real and imaginary parts of the dielectric constant.

$$\varepsilon_{complex} = \frac{i}{w}\sigma_{complex} \tag{2.49}$$

Where we defined complex conductivity as

$$\sigma_{complex} = \sigma - i\varepsilon\omega \tag{2.50}$$

The complex dielectric function and complex conductivity are connected to laboratory-measured observables such as absorption as well as solid-material characteristics such as effective mass and carrier density. Consider a wave propagating in the z-direction to determine these relations. By placing K in equation (2.43), we get a plan wave in the form

$$\vec{E}\ (z,t) = E_0\ e^{i\omega t}\ e^{\left(i\omega z\sqrt{\varepsilon\mu}\sqrt{1+\frac{i\sigma}{\varepsilon\omega}}\right)} \tag{2.51}$$

For free space, $\varepsilon = \varepsilon_0$, $\mu = \mu_0$, and $\sigma = 0$. The equation (2.51) is reduced to a simple plane wave solution.

$$\vec{E} = E_0\ e^{i(Kz-\omega t)} \tag{2.52}$$

Here, $K = K_0 = \omega\sqrt{\mu_0\varepsilon_0}\ and\ c = \frac{1}{\sqrt{\mu_0\varepsilon_0}}$, since c is the speed of electromagnetic wave in free space.

If the electromagnetic wave propagates in a material with finite electrical conductivity, the equation (2.51) can be expressed in form as follows:

$$\vec{E}\ (z,t) = E_0\ e^{-\frac{i\tilde{k}z}{c}}\ e^{i(\frac{\omega\tilde{n}z}{c}-\omega t)} \tag{2.53}$$

Since fi and k are the real and imaginary components of the complex refractive index, respectively, which can be described as:

$$\tilde{N}_{complex} = c\sqrt{\mu\varepsilon_{complex}} = c\sqrt{\mu\varepsilon(1+\frac{i\sigma}{\varepsilon\omega})} = \tilde{n}\ (\omega) + i\ \tilde{k}\ (\omega) \tag{2.54}$$

Here the real part $\tilde{n}$ is the refractive index which is defined as the ratio between the speed of light in free space and the speed of light in the medium [40]. The imaginary part $\tilde{k}$ is called extinction coefficient which determined the amount of light absorbed at a given wavelength [41].

The dispersion equation, defined by the following relations, introduces the complex refractive index formula [42]:

$$N_{complex} = \tilde{n}\ (\omega) + i\ \tilde{k}\ (\omega) \tag{2.55}$$

$$= (\varepsilon_r + i\ \varepsilon_{im})^{\frac{1}{2}} \tag{2.56}$$

Where ε_r and ε_{im} are the real and imaginary dielectric constants. The effective dielectric constant ε_{eff} is expressed in terms of the real part ε_r and imaginary part ε_{im}, through the relation [43]:

$$\varepsilon_{eff} = \varepsilon_r + i\,\varepsilon_{im} \tag{2.57}$$

It also expressed in terms of the refractive index $\tilde{n}(\omega)$ as following [43]:

$$\varepsilon_{eff} = \tilde{n}^2(\omega) \tag{2.58}$$

Squaring both sides of equation (2.56), and comparing the real and imaginary parts on both sides of the equation, we can get ε_r and ε_{im} in terms of $\tilde{n}(\omega)$ and $\tilde{k}(\omega)$

$$\tilde{n}^2(\omega) - \tilde{k}^2(\omega) = \varepsilon_r \tag{2.59}$$

$$2\,\tilde{n}(\omega)\,\tilde{k}(\omega) = \varepsilon_{im} \tag{2.60}$$

2.3.7 Drude - Lorentz model

Drude and Lorentz developed a classical theory of the refraction and dielectric constant of materials as they relate to light frequency. The Drude-Lorentz model explains dielectric dispersion. Starting with the equation of motion for a system of particles subjected to a resistive force while motion, we can define the equation of electron motion as follows [39]:

$$m\frac{d^2x}{dt^2} + \frac{mv}{\tau} = e\,E_0 e^{-i\omega t} \tag{2.61}$$

Where m is the mass of the electron, $\frac{d^2x}{dt^2}$ is the electron acceleration, $\frac{mv}{\tau}$ is the damping force of the medium and the sinusoidally time dependent electric field. As the applied electric field is sinusoidal, the electrons will experience the following sinusoidal motion:

$$\frac{dx}{xt} = v = v_0 e^{-i\omega t} \tag{2.62}$$

By taking the derivative for both sides, we can get:

$$\frac{dx^2}{dt^2} = \frac{dv}{dt} = v_0(-i\omega)e^{-i\omega t} \tag{2.63}$$

Now, substituting equation (2.62) and (2.63) into equation (2.61):

$$m\, v_0(-i\omega)e^{-i\omega t} + m v_0 e^{-i\omega t} = e\, E_0 e^{-i\omega t} \tag{2.64}$$

Therefore, we can write:

$$v_0 = \frac{eE_0}{\frac{m}{\tau} - im\omega} \tag{2.65}$$

Since the current density, which is related to the carrier density and the drift velocity, is defined as:

$$\vec{J} = nev_0 = \sigma E_0 \tag{2.66}$$

Substituting equation (2.65) into equation (2.66) to get:

$$\sigma = \frac{ne^2\tau}{m(1 - i\omega\tau)} \tag{2.67}$$

Suppose that the only conduction mechanism we are working on at that point is the free carrier mechanism. Therefore, in order to determine the entire complex dielectric function, we will take into account all other contributions to o in terms of ε_{core} doping impurity (core dielectric constant)

$$\varepsilon_{complex} = \varepsilon_{core} + \frac{i\sigma}{\omega} \tag{2.68}$$

Substituting equation (2.67) into equation (2.68) to get:

$$\varepsilon_{complex} = \varepsilon_{core} + \frac{i}{\omega}\frac{ne^2\tau}{m(1-i\omega\tau)} . \frac{1+i\omega\tau}{1+i\omega\tau} = \varepsilon_r + i\varepsilon_{im} \tag{2.69}$$

Then we can written the real and imaginary part of dielectric constant as:

$$\varepsilon_r = \varepsilon_{core} - \frac{ne^2\tau^2}{m(1+\omega^2\tau^2)} \tag{2.70}$$

$$\varepsilon_r = \frac{ne^2\tau}{\omega m(1+\omega^2\tau^2)} \tag{2.71}$$

Chapter Three

Experimental details

3.1 Glass cleaning

At first, the glass substrate with dimension (25.4 x 76.2 x 1.2 mm), which is used for thin film deposition, is cleaned by a soft sponge, distilled water, and alcohol to remove impurities, dust, and proteins from the surface. Some of these glasses are split evenly into small 30 mm pieces by the glass cutter before cleaning. The cleaned glasses were then placed in a beaker filled with ethyl alcohol (97%). They were subsequently washed in alcohol and dried. Finally, we check that there are no scratches or cracks on the glasses' surfaces before using them as clean substrates for our work.

3.2 Thin film preparation

The sputtering (Fig. 3.1) technique is used for the formation of the optically transparent windows. 50 nm-thick SiO_2 films are prepared by running the ion coater for 300 s. Some of the fabricated SiO_2 films are used as a substrate to deposit thin layers of Gold for 30 s per round, which deposit layer with a thickness of 50 nm, and repeated the rounds two and four times to have a thickness of Au layer of 100 and 200 nm in order to obtain optical properties. Then it was covered with another layer of SiO_2 with a thickness of 50 nm, which is shown in Fig. 3.3. During this process, the system is closed completely. The optical images of real samples are shown in Fig. 3.2. For the purpose of investigating the surface morphology, the top surfaces of SiO_2 films were coated with Au nanosheets of thickness of 50, 100, and 200 nm.

Fig. 3.1: The ion coater sputtering system

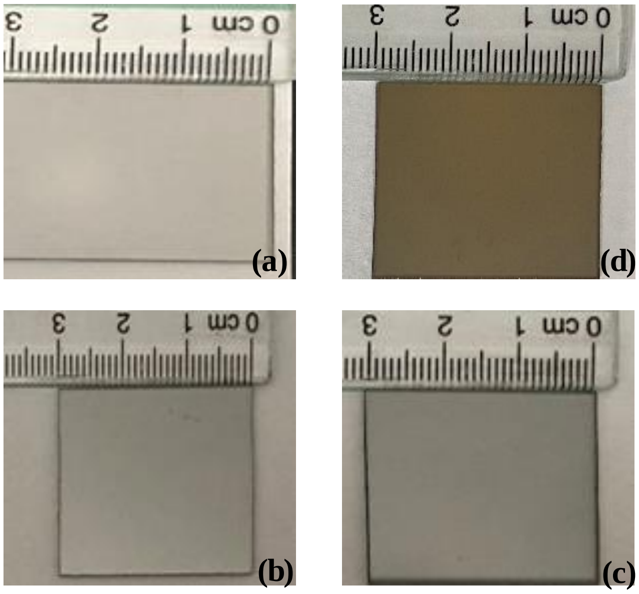

Fig. 3.2: The optical images of real samples of (a) SAS-00 (b) SAS-50 (c) SAS-100 (d) SAS-200

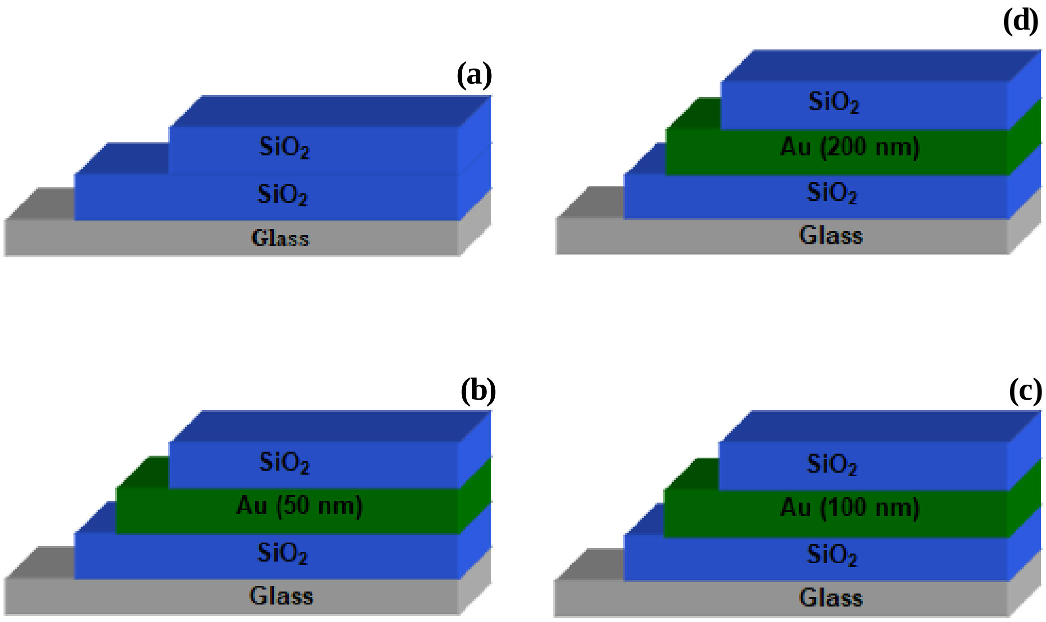

Fig. 3.3: The geometrical design of the real films of (a) SAS-00, (b)SAS-50, (c)SAS-100, and (d)SAS-200

The thickness of the SAS samples was determined using a surface roughness tester-profilometer (Model SOLID TR-200 plus). The SAS-00, 50, 100, and 200 have an average readings of around 100, 150, 200, and 300 nm, according to the profilometer. The error percentage in the measured values was ~ 10%. Fig. 3.4 depicts the roughness tester-profilometer (Model SOLID TR-200 Plus) system.

Fig. 3.4: The roughness tester-profilometer (Model SOLID TR-200 Plus) system.

3.3 Thin film analysis

The thin film analysis were carried out using hot prop, the X-ray diffraction, the scanning electron microscopy, and optical spectroscopy technique to explore the conductivity type, the structural, the morphology, and the optical properties of the films, respectively.

3.3.1 The hot probe technique

The hot probe technique is used to determine the conductivity (σ) type of semiconductors, which is required for electric applications. In this technique if the semiconductor is n-type, that means that the majority carrier is an electron, while if it is p-type, the majority carrier is a hole. The setup for this process involved touching the produced sample with a heat soldering iron (hot probe) and a cold probe, as shown in Fig. 3.5, the heat source will cause charge carrier motion, which will cause a current/voltage difference [44]. The digital multimeter connects both probes. The hot iron was linked to the DMM's positive terminal, and the cold iron to the negative terminal. When the voltage reading on the DMM is positive, the semiconductor is n-type, which indicates that the material has a high concentration of electrons. The p-type semiconductor gives negative voltage values. When we did this test on our samples, we found that SAS-00 is p-type, SAS-50 is p-type, SAS-100 is n-type, and SAS-200 is n-type.

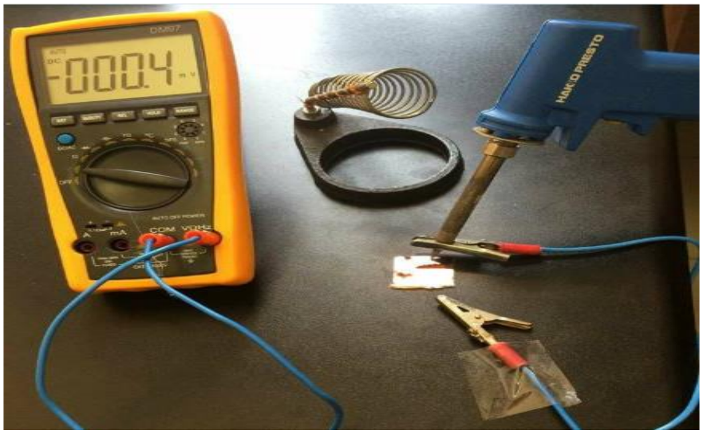

Fig. 3.5: The hot probe technique.

3.3.2 The X-ray diffraction measurements

XRD measurements were carried out using a Rigaku MiniFlex-600 X-ray power diffractometer (Fig. 3.6) with copper anode Kα radiation running at a voltage of 40 kV and a current of 15 mA. The 2θ scanning approach was used in the range of 10°-70°, with a scan rate of 1°/min with an average wavelength of 1.5405 A°. X-ray diffraction reveals the lattice structure of SAS-00, 50, 100, and 200. The diffraction patterns were investigated using Bragg's diffraction formula ($n\lambda = 2d \sin \theta$) with d being the distance between the oriented planes, and 2θ denotes the locations of the diffraction peaks. The system includes a monochromator, detector, slit set, and sample container. The sample rotates by 2θ, and the detector measures the intensity of the x-ray beam. Slits are also employed to adjust the x-ray beam's size and shape.

Fig. 3.6: Rigaku MiniFlex-600 X-ray power diffractometer.

3.3.3 Scanning electron microscope

To explore the surface morphology, the top surfaces of SAS-00, 50, 100, and 200 films, which were deposited onto glass substrates, were coated with an Au layer by the ion coater. The scanning electron microscope used for this purpose is shown in Fig. 3.7. The samples were installed inside the microscope using copper adhesive to make electrons flow into the surface. An electron gun produces a highly focused electron beam that the SEM uses to scan the film's surface. Through their interactions with the sample atoms, these electrons produce signals that provide details about the composition of the sample. A secondary electron detector is used to collect these secondary electrons from each site on the sample in order to produce a two-dimensional picture that illustrates the morphological properties of the designed film.

Fig. 3.7: Scanning electron microscopy (SEM).

3.3.4 The compositional measurements

Prepared sample composition is determined by using the energy dispersive X-ray spectroscopy (EDX) technique. By subjecting the sample to a high-energy electron beam, the electrons in the sample become excited to move from their inner to their outer shells, creating electron vacancies. When some electrons go from the outer to the inner shell, X-rays with an energy equivalent to the energy difference between the levels are released. Since the energy levels of electrons are quantized, the typical X-ray energy that each element emits varies often. The sample history will be utilized to identify the unknown beaks in situations where there is confusion regarding the peaks.

Fig. 3.8: The energy dispersive X-ray spectroscopy.

3.3.4 Optical measurements

The optical variables including the transmittance (T) and reflectance (R) were measured in the incident light wavelength range of 300-1100 nm at a scan rate of 1200 nm/min. The measurements were taken using a thermo-scientific Evolution 300 UV-Visible light spectrophotometer (Fig. 3.9). All measurement was handled at normal incidence. T% and R% are used to calculate absorption coefficients, interband transitions, optical energy band gaps, and band tails. The dielectric dispersion is also measured. The data is acquired using the VISION Pro software suite. The reflection coefficient was measured with help of Pike type reflectometer attached to the system. The measurements of the transmittance and reflectance were handled at normal incidence.

Fig. 3.9: Thermo-scientific evolution 300 UV-Visible light spectrophotometer

Chapter Four

Results and discussion

4.1 Structural analysis

The target of the current work is to enhance the electrical conductivity of a transparent electrode so that it allows optical transmittance and high electrical conductance at the same time. For this purpose, SiO_2 was selected. SiO_2-stacked layers of thickness 50 nm were sandwiched with Au nanosheets of thickness 50, 100, and 200 nm. The samples are named SAS-00, SAS-50, SAS-100,

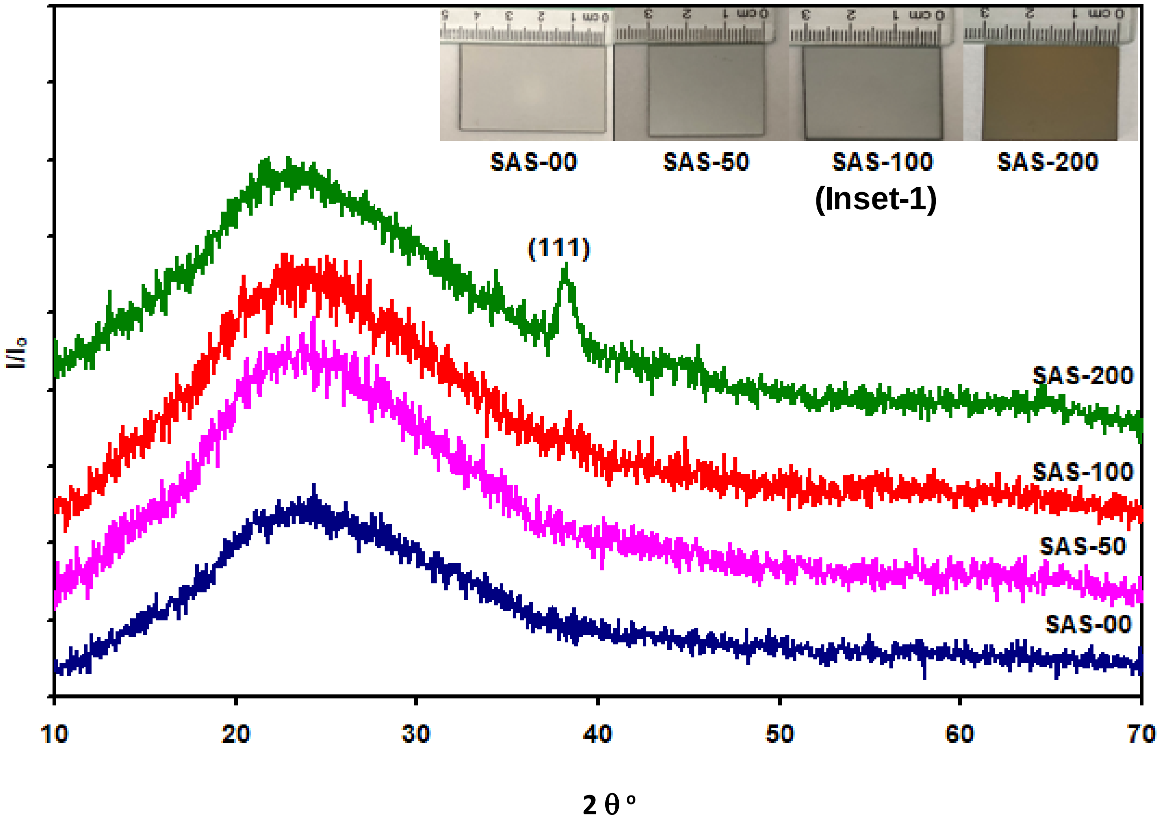

Fig4.1: The X-ray diffraction patterns for SiO_2/Au/SiO_2 with 0, 50, 100, and 200 nm thicknesses of Au, respectively. SAS-00, SAS-50, SAS-100, and SAS-200 show the optical image of the samples. Inset_1: Represent the optical images for real samples

and SAS-200, respectively. From Fig. 4.1 it is clear from the Inset_1 that the color of the film differs from sample to sample by increasing the thicknesses of the Au layer from 0 nm to 200 nm,

which have a water-like color and then become gray at a thickness of 50 nm of Au, then have a dark gray color at 100 nm, and finally acquire a golden color when the thickness of the Au layer is 200 nm. The X-ray diffraction (XRD) patterns for the SiO_2 / Au / SiO_2 film are displayed in Fig. 4.1. It is seen from the figure that the SAS films are amorphous in nature, as evidenced by the nonintensive XRD patterns. The peak that appeared in the SAS-200 films is assigned to Au (JCPDS Card No.04-0784). The peak appeared at $2\theta = 38.3^{o}$. This peak is assigned to FCC (Face Centered Cubic) gold being oriented along the (111) direction [45] ; its existence means that the film became gold rich.

4.2 Scanning electron microscopy

Scanning Electron Microscopy (SEM) was used to investigate the surface morphology of SAS-50, SAS-100, and SAS-200. In Fig. 4.2.a, the surface morphology of the SAS-50 film is represented. For an enlargement of 10K times, the gold nanoparticles are randomly distributed and accumulated in groups, and tiny particles with irregular shapes can be observed. On the other hand, by increasing the thickness of Au to 100 nm from an enlargement of 20K times shown in Fig. 4.1.b, some rarely observed circular grains appeared on the surface of the film. Moreover, Fig. 4.2.c represents the surface morphology of the film comprising a 200 nm thickness of Au. For an enlargement of 5K times, the accumulation of circular clusters has one core and appears to surround tiny spherical grains. Further enlargement by 10K, which is shown in Fig. 4.2.d, displays a larger sphere with a central core and surrounding tiny spherical grains of average size in the range of 0.9 – 2.0 µm. The average size of circular grains is 1.45 µm.

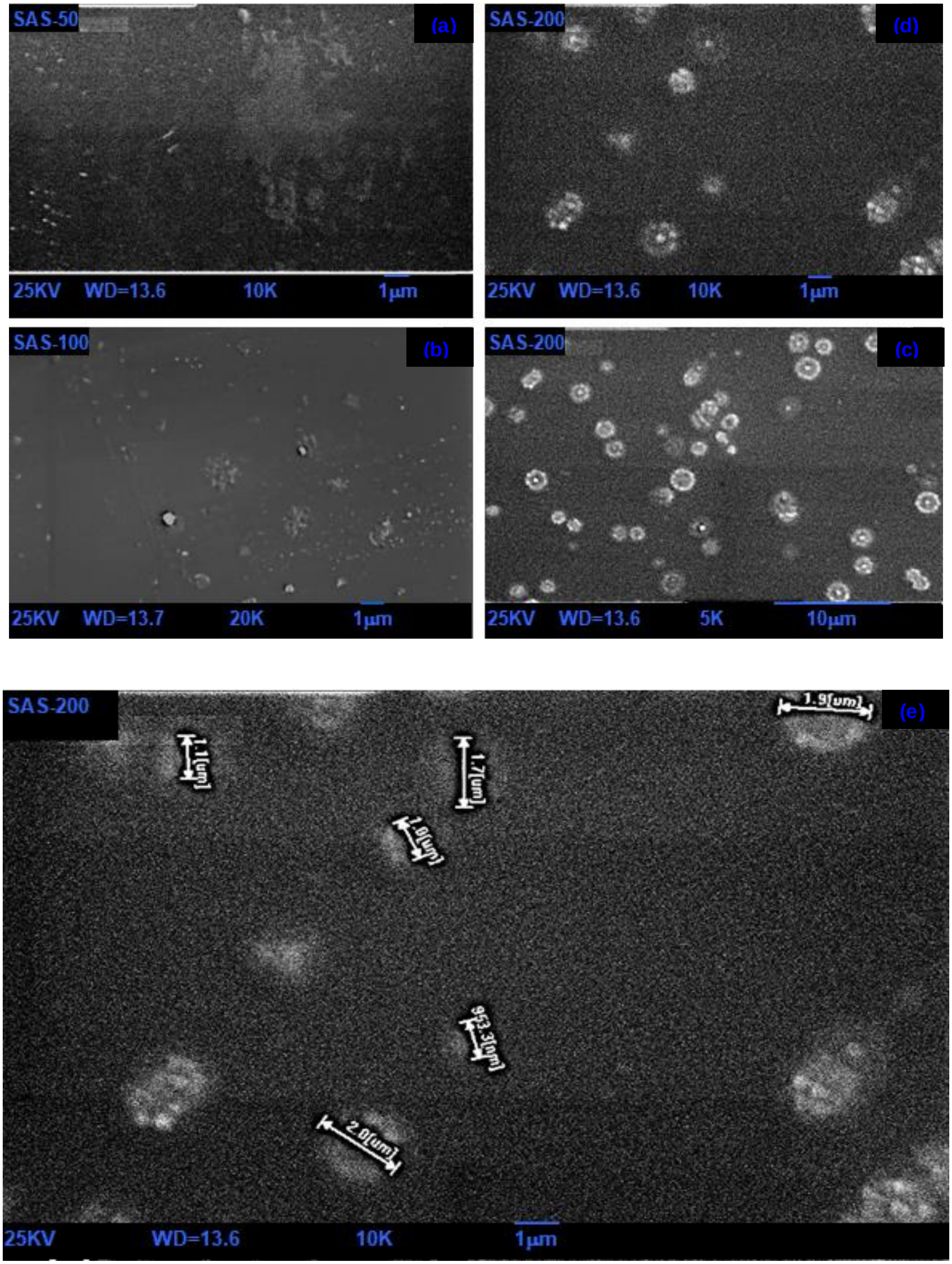

Fig4.2 : SEM image for sample.(a) SAS-50, (b) SAS-100, (c) SAS-200 5K enlargement, (d) SAS-200 10K enlargement films, and (e)SAS-200 10K enlargement measured.

4.3 Energy dispersive X-ray spectroscopy (EDS)

The energy dispersive X-ray spectra for SAS-00, SAS-50, SAS-100, and SAS-200 are presented in Fig. 4.3. As seen from the figure, the spectra indicate the presence of glass (SiO_2 : Na_2O : MgO : CaO) and Au. It is evident from the inset_1 shown in the figure that the content of Au increases with increasing Au thickness. The higher the Au concentration, the freer the electron concentration in the films. [46]

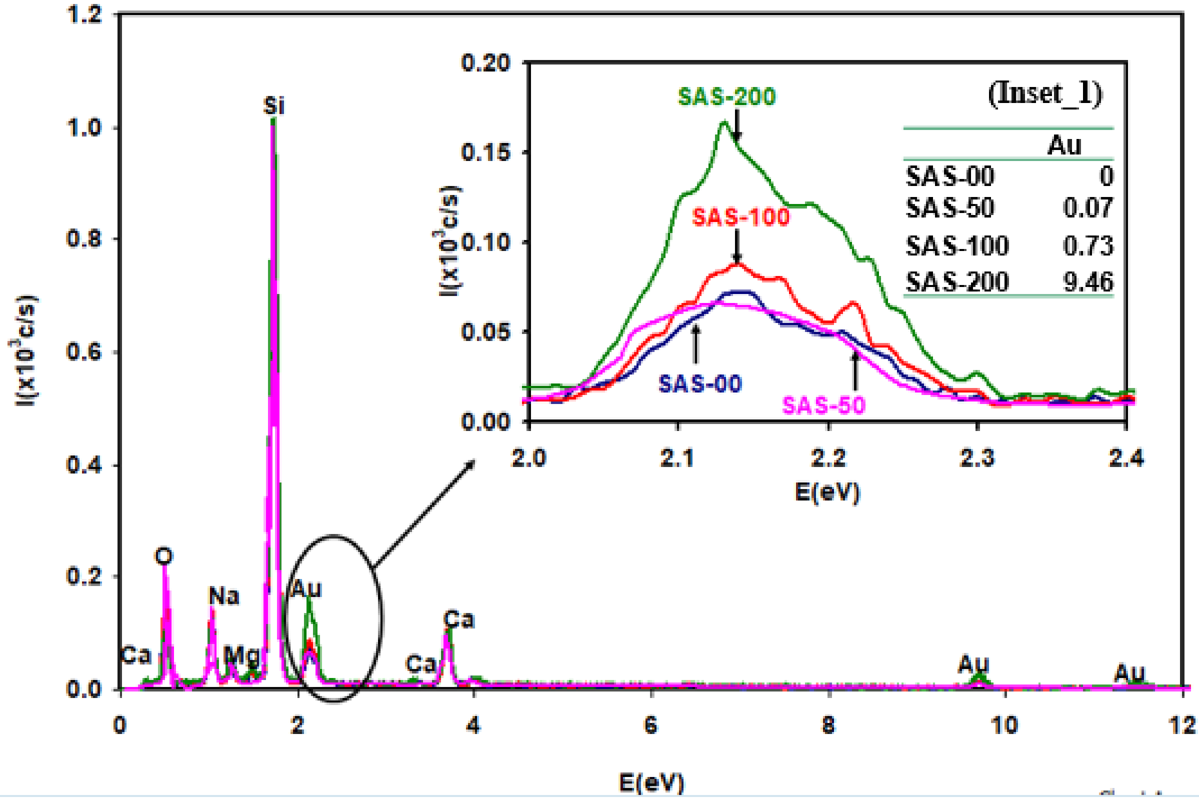

(Inset_1)

	Au
SAS-00	0
SAS-50	0.07
SAS-100	0.73
SAS-200	9.46

Fig. 4.3: The EDS for SAS-00, SAS-50, SAS-100, and SAS-200 films.
Inset_1: Represent the concentration of Au in the samples.

4.4 Optical analysis

In order to investigate the optical properties of SiO_2-stacked layers comprising slabs of Au, the optical transmittance (T) and reflectance (R) spectra were recorded. The measurements were carried out in a wavelength (λ) range of 300–1100 nm at a scanning speed of 1200 nm/min. The results are presented in Fig. 4.4. It’s clear from the figure that the transmittance spectra of SAS-00 sharply increase with decreasing energy below 3.6 eV, and then T saturates at 70%. Similarly, for SAS-50, the T% value increases with decreasing energy below 3.6 eV, then slightly decreases after reaching 2.5 eV. However, it saturates at 62%. On the other hand, by increasing the thickness of the Au layer to 100 nm, the transmittance sharply increased with decreased energy until the highest transmission value of 60.8% at 2.44 eV was reached, then the transmittance sharply decreased with further energy decreases. Likewise, when the thickness of the Au layer is increased to 200 nm, the transmittance slightly increases to a maximum value of 34.2% at 2.32 eV, then sharply decreases, reaching a minimum value of 8.36%. In general, the transmittance of SAS-100 and SAS-200 approximately shows the same behavior. The T% spectra of SAS-100 and SAS-200 indicate that the effect of the sandwiching of the Au layer between the SiO_2 layers becomes more effective when the energy of the incident light is less than 2.37 eV. Moreover, this decrease probably refers to increased light absorption [47] .In addition, the increased thickness of the Au layer increases the free carrier concentration [48], leading to a higher plasmon interaction [49]. .For energy conservation, the low infrared transmittance thin films were advantageous.[50]

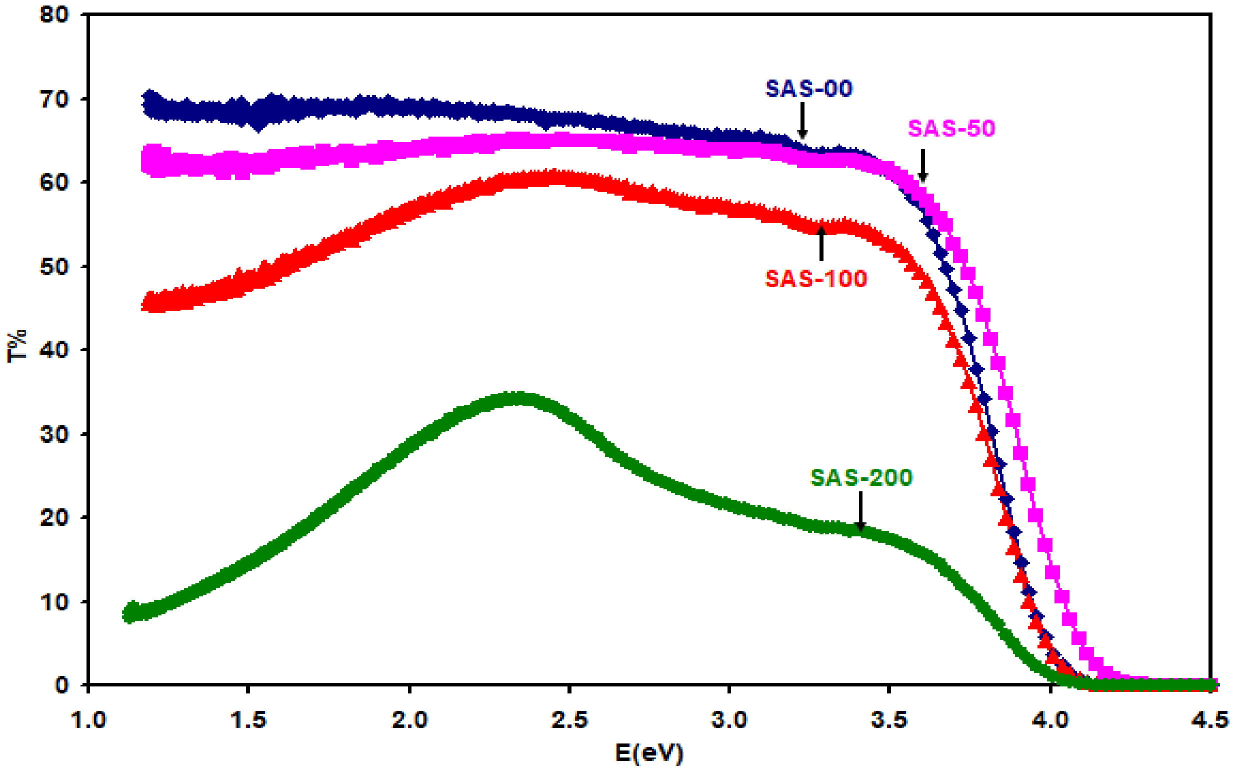

Fig. 4.4: The transmittance spectra for SAS-00, SAS-50, SAS-100, and SAS-200 substrates, respectively, are in the range of 1.13-4.50 eV.

On the other hand, the reflectance (R) spectra for SAS-00, 50, 100, and 200 are illustrated in Fig. 4.5. The reflectance slowly increases with decreasing energy until an energy value of 1.48 eV is reached. The reflectance of SAS-00, 50, and 100, which is present in Fig. 4.5 (a). For smaller energy values, the reflectance of SAS-00, 50, and 100 rapidly increases with decreasing energy. It is also remarkable from Fig. 4.5 (b) that the reflectance spectra of the SAS-200 display a slow increase in R% value until 15.6% at 2.43 eV, then rapidly increase from 15.6% to 54.8% at energies equal to 2.43 and 1.16 eV, respectively. The abnormally increased R values should play a role in enhancing the dielectric properties. It means that SAS-200 substrates are suitable for high-dielectric gate applications [51]. While probable reasons laying beyond the increased reflectance could be the increased scattering and increased surface roughness with an increased Au layer [52][53][54][55].

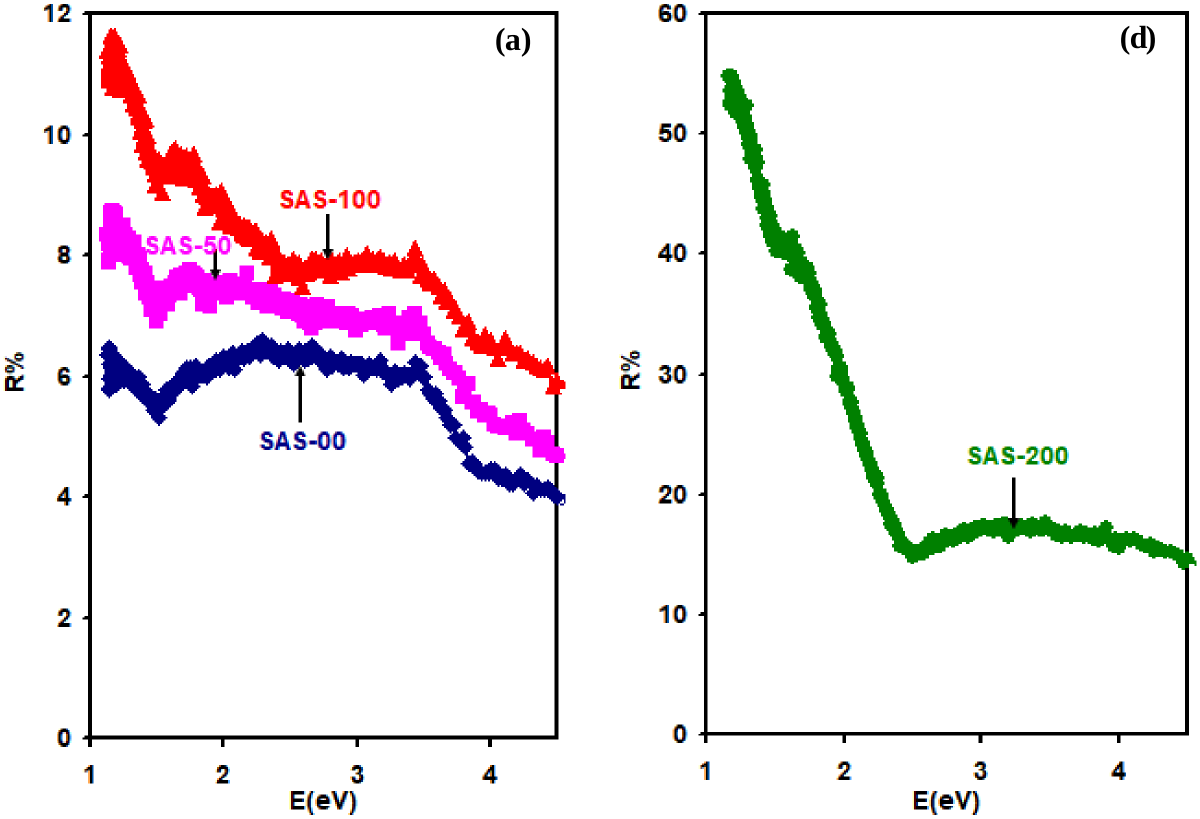

Fig. 4.5: The reflectance spectra (a) for SAS-00, SAS-50, SAS-100, and (b) SAS-200 substrates, respectively, in the range of 1.0-4.5 eV.

The optical transmittance and reflectance coefficients are used to calculate the absorption coefficient (α) form equation (2.9) for SAS-00, 50, 100, and 200 samples. The absorption coefficient is shown in Fig. 4.6. It is clear from the figure that the absorption coefficient in the spectral range of 3.7 -4.5 eV for SAS-00 is relatively high compared to SAS-50, 100, and 200 interfaces. While the absorption coefficient for all samples decreases with decreasing incident photon energy, clearly, the α- spectra in the infrared range are illustrated in inset-1 of Fig. 4.6. It is observed that they remain constant, then slightly increase by decreasing the incident photon energy (E) in the range (1.40 - 1.80) eV and increasing the thickness of the Au layer, resulting in the generation of electrons that act as a source of free charge carriers. It is usually ascribed to the free carrier absorption mechanisms that attribute it to material that has metal-like properties. However, the free carrier absorption in the low energy range mostly results from impurities [56], carrier transitions between conduction and valence bands [57], defects [58], and increasing the thickness of the Au layer as mentioned. Particularly, the rate of change of α with E ($\frac{\Delta\alpha}{\Delta E}$) for SAS-00, 50, 100, and 200 are -0.547, -0.386, -1.794, and -3.529, respectively. Therefore, it is evident that the increase in the thickness of the Au layer leads to a different set of band tails that narrows with increasing Au concentration.

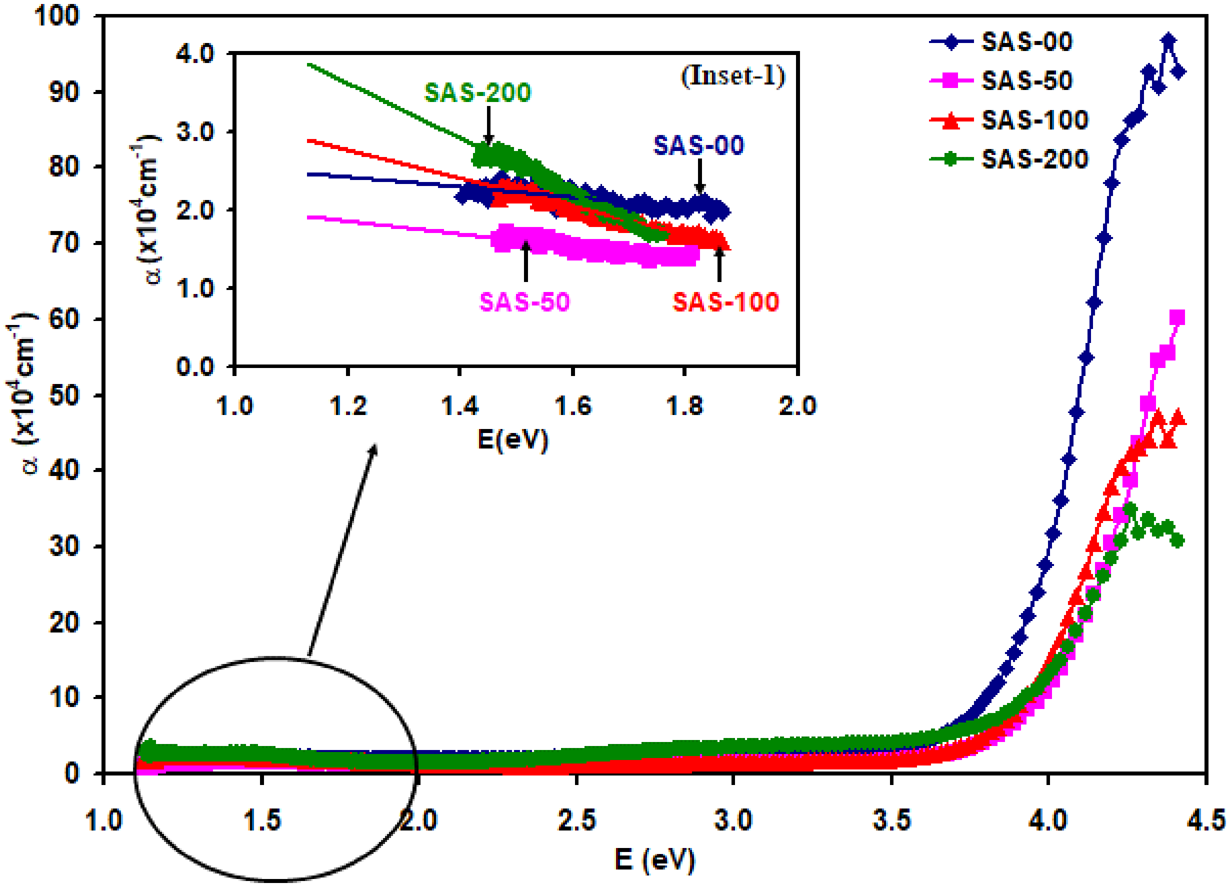

Fig. 4.6: The absorption coefficient spectra for SAS-00, SAS-50, SAS-100, and SAS-200 are in the range of 1.0 - 4.5 eV.

To explore the effect of the Au layer on the optical transitions in SAS-xx samples, Tauc's equation (2.10) was employed. The respective $(\alpha\ E)^2$, $(\alpha\ E)^{2/3}$, $(\alpha\ E)^{1/2}$, and $(\alpha\ E)^{1/3}$ versus E variation were plotted as illustrated in Figs. 4.7, 4.8, . 4.9, and 4.10, respectively. Then they were compared. The most appropriate fit of the data for all samples was obtained for the $(\alpha\ E)^{1/3}$ – E variation, indicating that the band gap is of the indirect forbidden transition type. The intercept of the E-axis revealed an energy band gap value, which indicates a decrease in the energy band gap that is present in Table 4.1. However, the decrease in the value of the band gap is due to increasing thickness of the Au layer, which reduces the Urbach energy in the optical band and is probably attributed to the increased structural disorder [59].

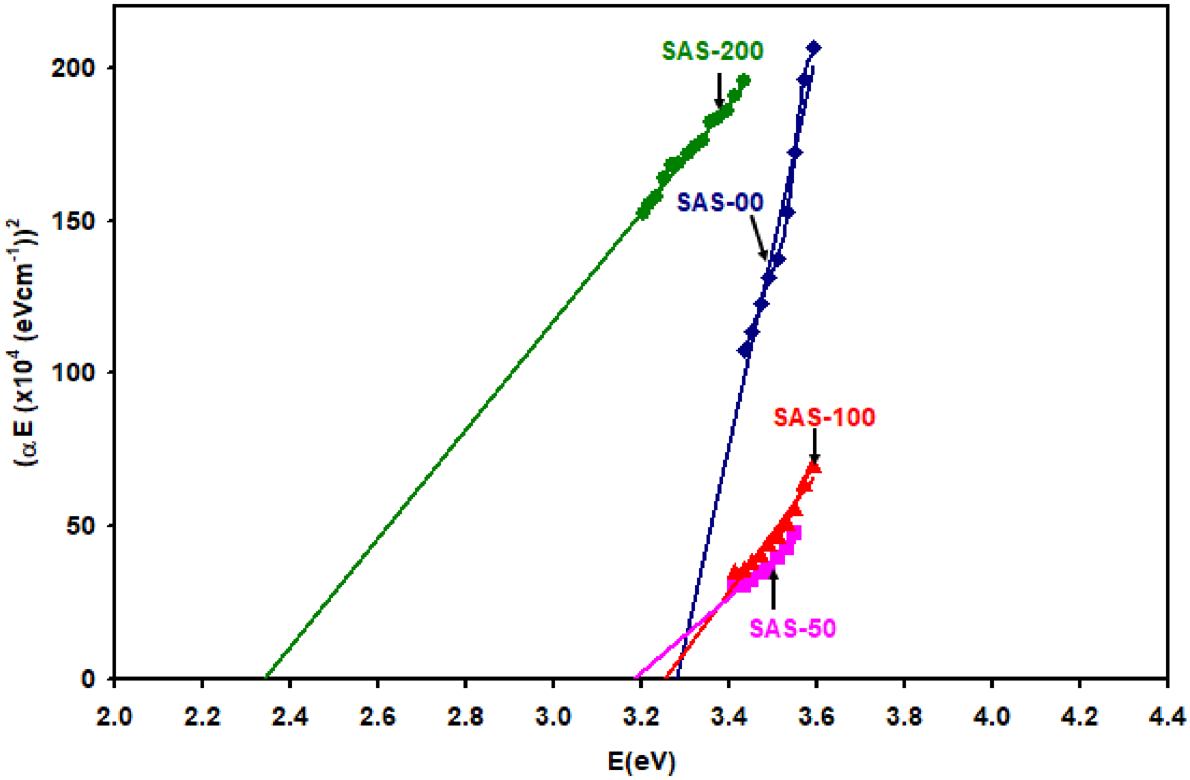

Fig. 4.7: The energy band gap for SAS-00, SAS-50, SAS-100, and SAS-200 was in the range of 2.0- 4.4 eV.

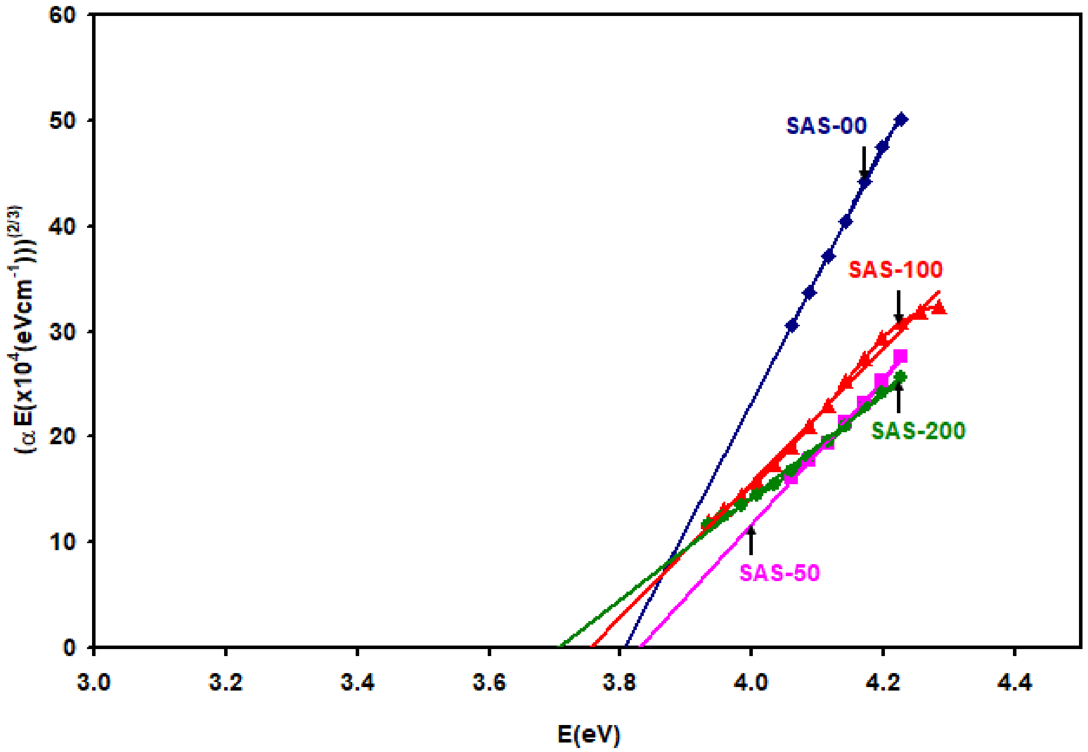

Fig. 4.8 : The energy band gap for SAS-00, SAS-50, SAS-100, and SAS-200 was in the range of 2.0- 4.4 eV.

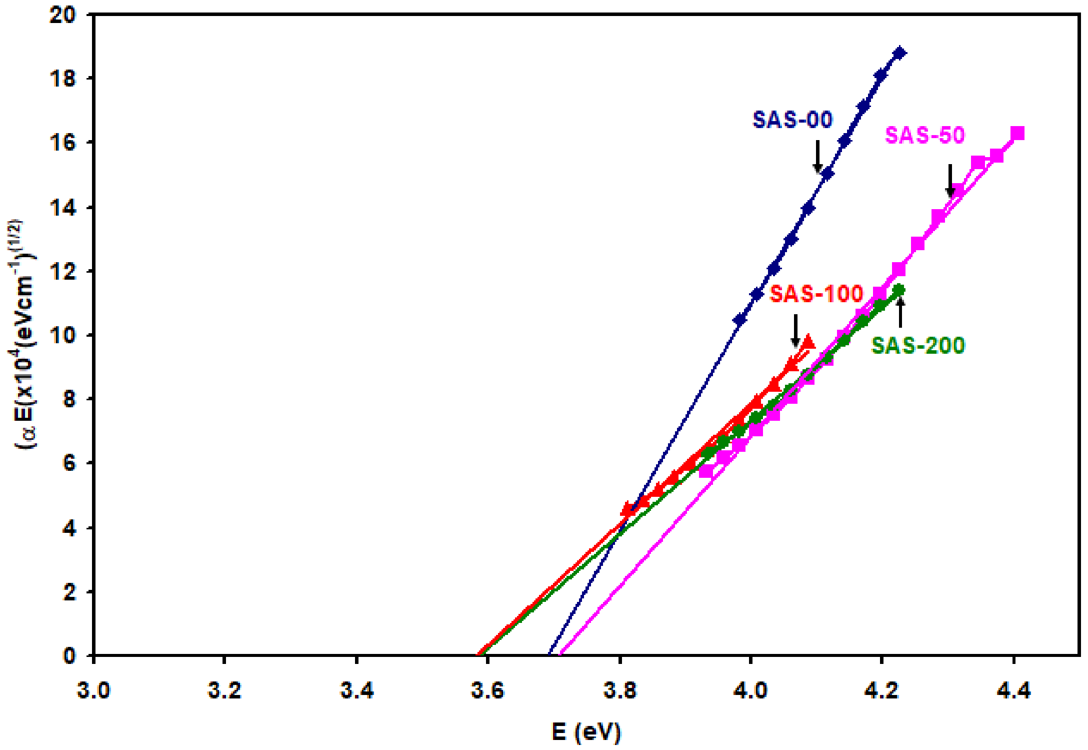

Fig. 4.9 : The energy band gap for SAS-00, SAS-50, SAS-100, and SAS-200 was in the range of 3.0- 4.6 eV.

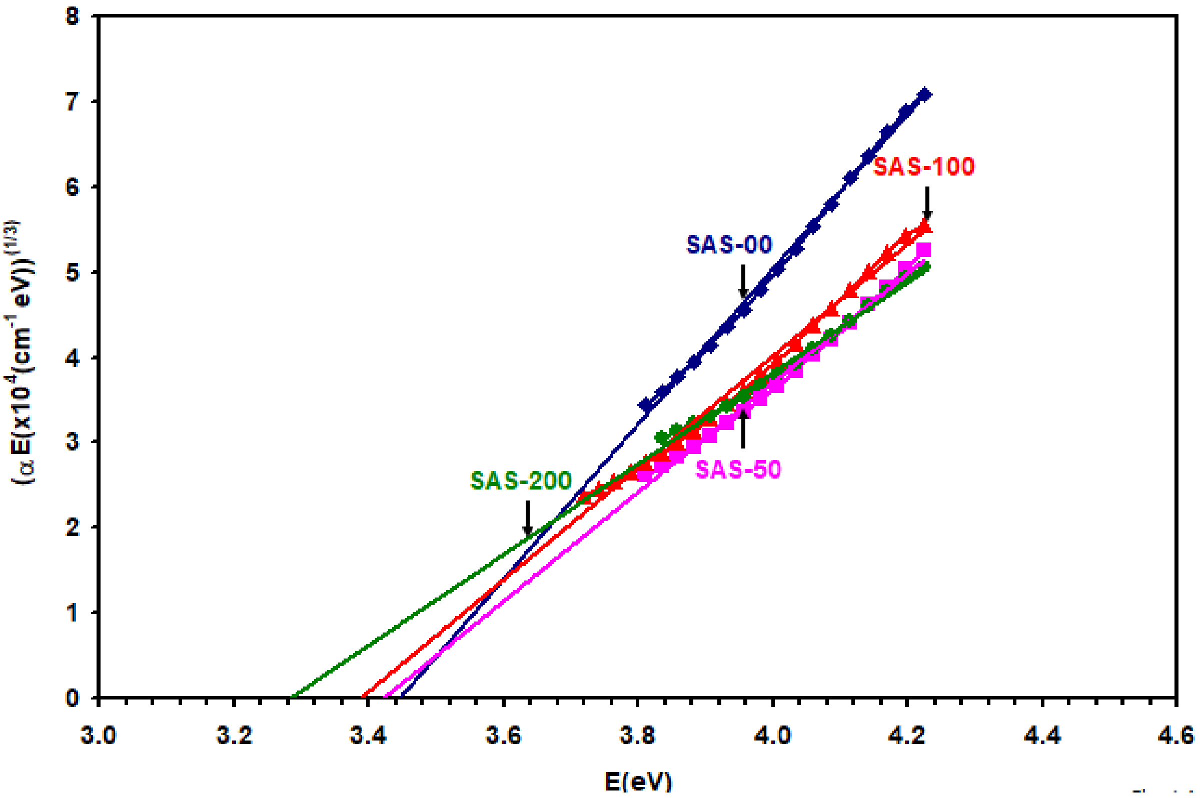

Fig. 4.10: The energy band gap for SAS-00, SAS-50, SAS-100, and SAS-200 was in the range of 3.0- 4.6 eV.

Additionally, this red shift in band gap energy results from the generation of new electronic states within the conduction and valence bands, which decreases the value of E_g [60, 61]. The decreases in band gap is advantageous for optoelectronic application [62] SiO_2 films correspond to bonds of Si-O of length 1.6 A° [63]. The bonding is created between Si^{+4} and four O^{-2} atoms to form corner-sharing SiO_4 tetrahedra. The fundamental band gap of it is 9.57 eV, showing valance band maxima (VBM) at (½, ½, ½) of the cubic cell. The conduction band minima (CBM) is at the lattice center (0, 0, 0). VBM mainly comes from O-2p and Si-3p; however, CBM is not directed orbitals above VBM it can result from 3p orbits up to 3d of the Si atom [64]. This feature provides a wide variety in the energy band gap value.

Urbach energy values for SAS-00, 50, 100, and 200 were determined in the range of 1.19–1.50 eV. The Urbach energy can appear due to defects [65, 66] and low crystallinity in the films [67]. Urbach energy (E_u) was estimated from equation (2.30) by plotting ln (α) vs. incident photon energy and fitting the slope of the curve as shown in Fig. 4.11. It is clear from the linearity of slopes that the band tails exist in SAS-00 and SAS-50. The band tail width for all samples is illustrated in Table 4.1. It's noticeable from the table that the values of band tail width for SAS-00 and SAS-50 exhibit values lower than $E_g/2$. The rule is not valid for SAS-100 and SAS-200. It is clear that the two samples exhibit metal-like orbital overlapping. Strong orbital overlapping guaranteed by the thicker Au layer shifts the band gap tails closer to the conduction band minima. Such a shift leads to a shift of the fermi level to the conduction band, showing degenerate semiconductor characteristics.

Table 4.1: The energy band gap and the energy band tails for SAS-00, 50, 100, and 200

	SAS-00	SAS-50	SAS-100	SAS-200
E_g (eV)	3.48	3.45	3.41	3.28
E_u (eV)	1.385	1.217	-	-

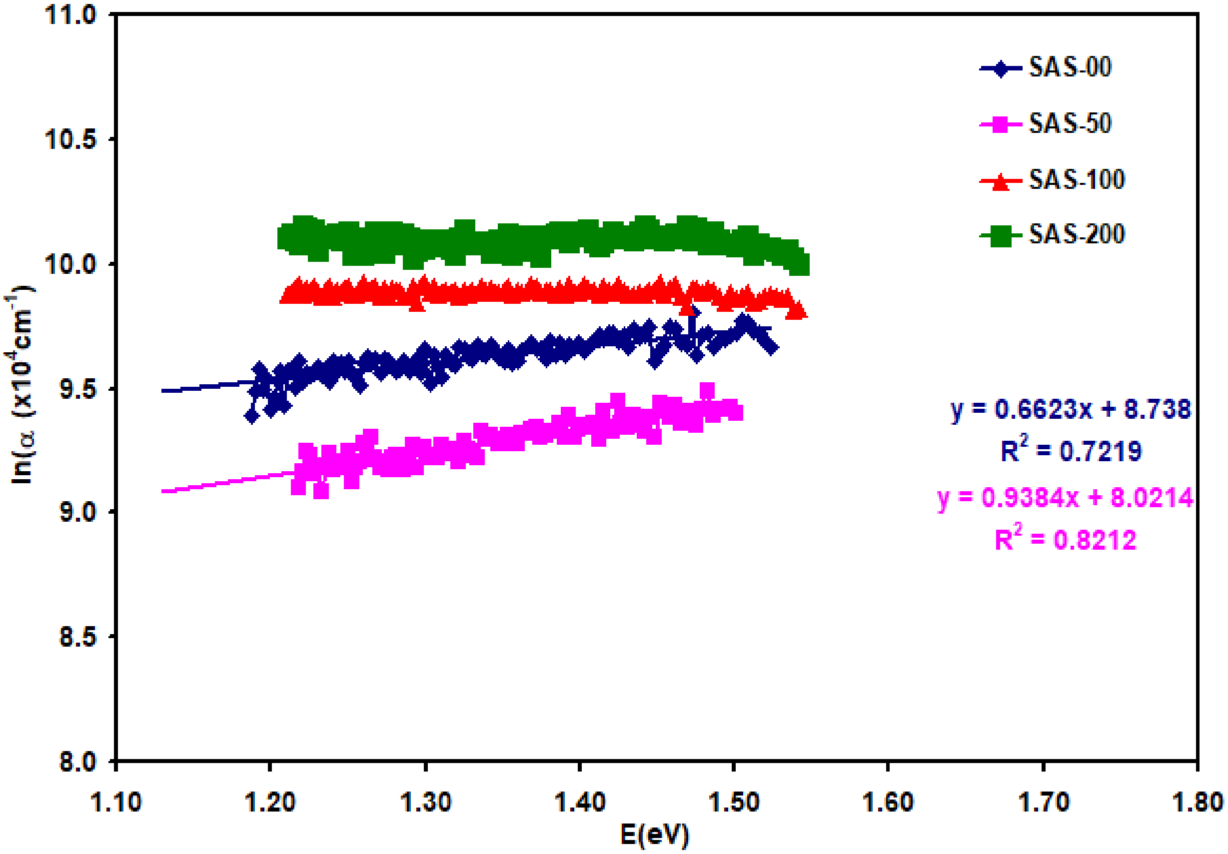

Fig. 4.11: ln (α) VS photon energy spectra

4.5 Dielectric properties

To expand the possible application of this structure, dielectric properties are investigated. The optical transmittance and reflectance spectral data were used to determine the dielectric constant spectra of the films. Fig. 4.12 and Fig. 4.14 display the spectra of the real and imaginary parts of the dielectric constant, respectively. The dielectric constant spectra were calculated using (2.59) and (2.60). Fig. 4.12(a) shows that the SAS-00 has a low dielectric constant value of 2.83. Literature reported a low dielectric constant for SiO_2 with a value of 2.25 [68]. Moreover, by increasing the thickness of the Au layer by 50 or 100 nm, the dielectric constant increased to 3.37 for SAS-50 and 4.14 for SAS-100. However, by increasing the Au layer thickness to 200 nm in accordance with Fig. 4.9(b), the dielectric constant sharply increases, reaching an abnormal value of 44.9. The enhancement is that the dielectric constant spectra indicate the suitability of SAS samples for high-k-dielectric applications. In addition, this increase in ε_r value in the visible and infrared ranges can be attributed to free carrier absorption, which improves the dielectric properties by increasing the values from 2.83 to 44.9.It is also noted that the SAS-00 and SAS-50 samples show slow increases with decreasing incident photon energy values. The variation in the dielectric constant of SAS-100 becomes sharper in the IR range. It can also be observed from Fig. 4.9(b) that the dielectric constant of SAS-200 films shows very sharp increases in the spectral range of 1.15–2.50 eV. This property is regarded as an advantage for non-linear optical applications. Wide tunability of optical devices is possible due to the thin film trend of variation.

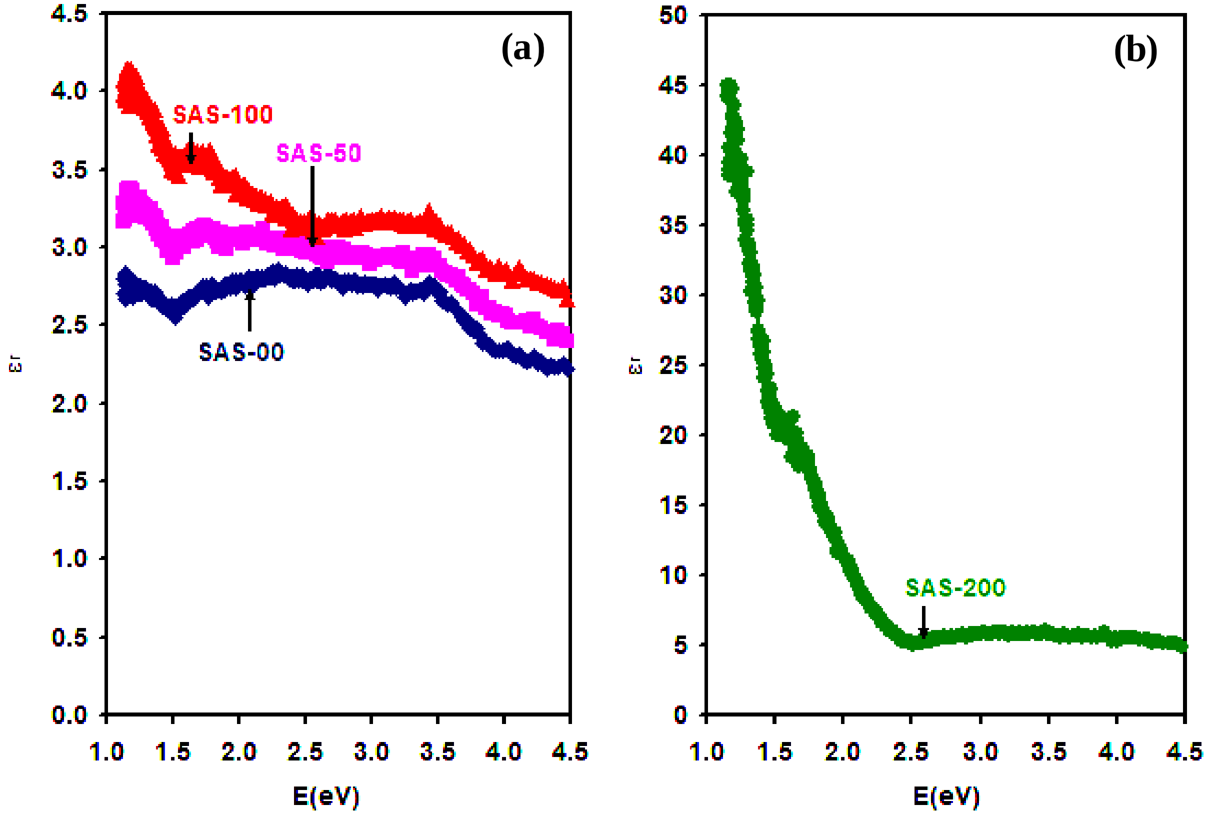

Fig. 4.12: (a) real parts of the dielectric constant of the SAS-00, 50, and 100 with energy, and (b) for the SAS-200.

The real part of the dielectric constant is modeled using equation (2.70) to investigate the properties of this dielectric medium by using the Drude-Lorentz model, where the fitting parameters are tabulated in Table 4.2 and as Fig. 4.13 illustrates. Here, the hole effective mass in SiO_2 is found to be 0.58 m_0, where m_0 is the free electron mass [69] and the effective mass of Au is 1.10 m_0 [70]. By increasing the thickness of the Au layer, ε_{core} (ε_∞) becomes larger, increasing from the value of 2.55 to 11 for SAS-00 and SAS-200, respectively. In addition, the optical parameters like τ, n, and μ are affected by this increase in the Au layer. For example, in the infrared region, the scattering time (τ) for SAS-00 was 1.1 fs; when we reach a thickness of 200 nm of the Au, it becomes 0.7 fs. The lower the scattering time constant, the higher the electronic friction coefficient. In addition, it is important to notice that the scattering time (τ) for SAS-00 in all energy regions is larger than its value for SAS-200, and the scattering time (τ) depends on the number of free carriers and the crystalline nature of the material. Particularly, the longer the scattering time, the lower the electronic friction in the material since the free carrier motion of the electrons through SAS-00 and SAS-50 is hardily possible because of their amorphous nature. Moreover, the rise in free carrier density caused by sandwiching the Au layer in the SiO_2 substrate reduces the drift mobility (μ) from 1.819 cm^2/Vs for SAS-00 to 0.691 cm^2/Vs for SAS-200 in the ultraviolet energy region. The free electron density in the ultraviolet region is found to be 8 $x10^{18}$ cm^{-3}, 9 $x10^{18}cm^{-3}$, and 7 $x10^{18}$ cm^{-3} for SAS-00, SAS-50, and SAS-100, respectively. Then it increased to a value of 600 $x10^{18}$ cm^{-3} when the thickness of Au layer reaches 200 nm. The increase in n values from 10^{18} to 10^{20} indicate that SAS-200 exhibit metal plate characteristic with high number of free electrons. The substrate with these properties can be used as electron source.

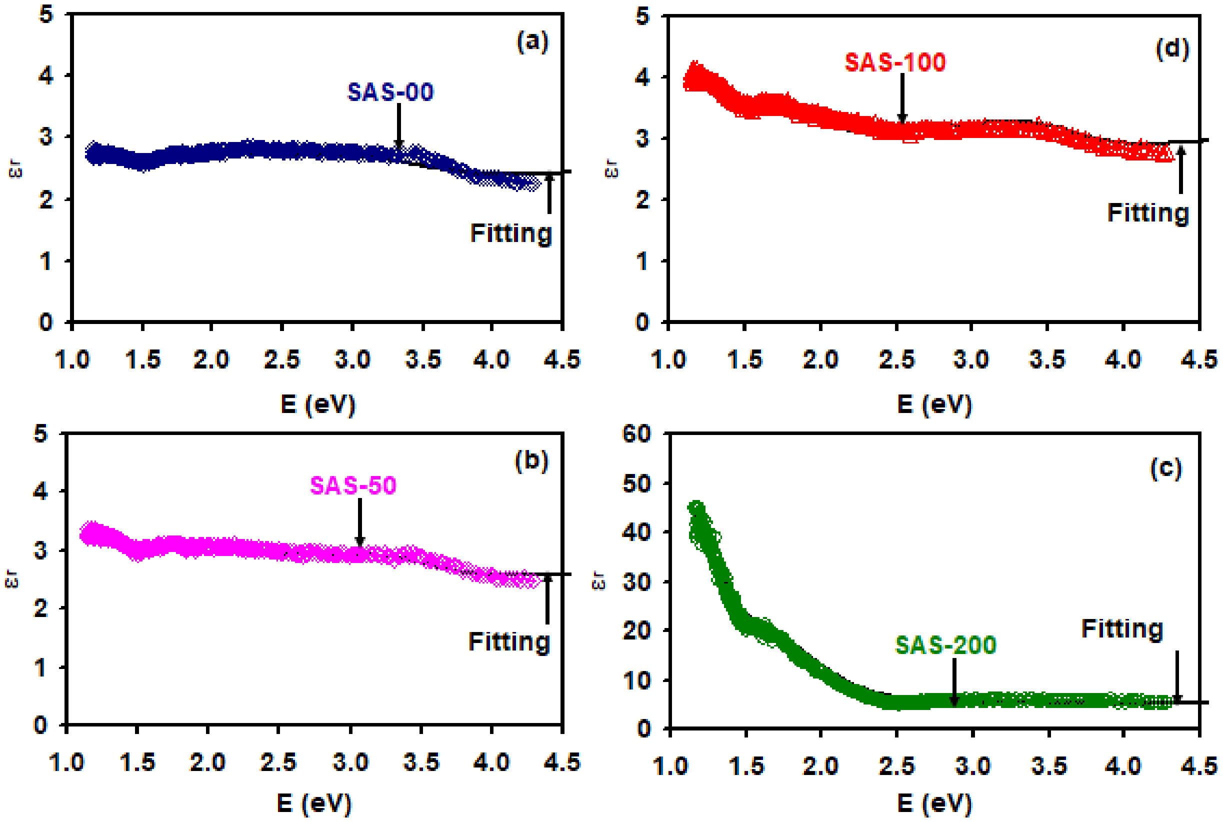

Fig. 4.13 : The real part of the dielectric spectra for (**a)** SAS-00,(**b)** SAS-50, (**c)** SAS-100, and (**d)** SAS-200.

The black-colored plots represent the fitting.

Table 4.2: The Optical Conductivity Parameters for SAS-00, 50, 100, and 200

sample	**SAS-00 m*/m = 0.29**			**SAS-50 m*/m = 0.229**			**SAS-100 m*/m = 0.229**			**SAS-200 m*/m = 0.229**		
parameter	**1**	**2**	**3**	**1**	**2**	**3**	**1**	**2**	**3**	**1**	**2**	**3**
E_∞	**2.55**			**2.8**			**3.2**			**11**		
E(eV)	**1.4**	**2.5**	**3.5**	**1.4**	**2.4**	**3.6**	**1.4**	**2**	**3.7**	**1.3**	**2**	**3.5**
τ (fs)	**1.1**	**0.8**	**0.3**	**1.2**	**0.5**	**0.3**	**1.1**	**0.4**	**0.4**	**0.7**	**0.3**	**0.09**
n ($x10^{18}cm^{-3}$)	**0.3**	**0.3**	**8**	**0.8**	**2**	**9**	**1**	**5**	**7**	**70**	**200**	**600**
μ (cm^2/Vs)	**6.669**	**4.850**	**1.819**	**9.213**	**3.839**	**2.303**	**8.446**	**3.071**	**3.071**	**5.375**	**2.303**	**0.691**

On the other hand, to get information about the optical conductivity ($\sigma(\omega) = (\varepsilon_{im}\,\omega/4\pi)$; ω is the angular frequency), the imaginary part (ε_{im}) of the dielectric constant spectra is measured. The ε_{im} for the SAS-00, 50, 100, and 200 are presented in Fig. 4.14. It is clear from the figure that the optical conductivity of the samples is increasing in the infrared range, which is evidence of an increase in the ε_{im}. The increase in conductivity can be attributed to an increase in the free carrier concentration.

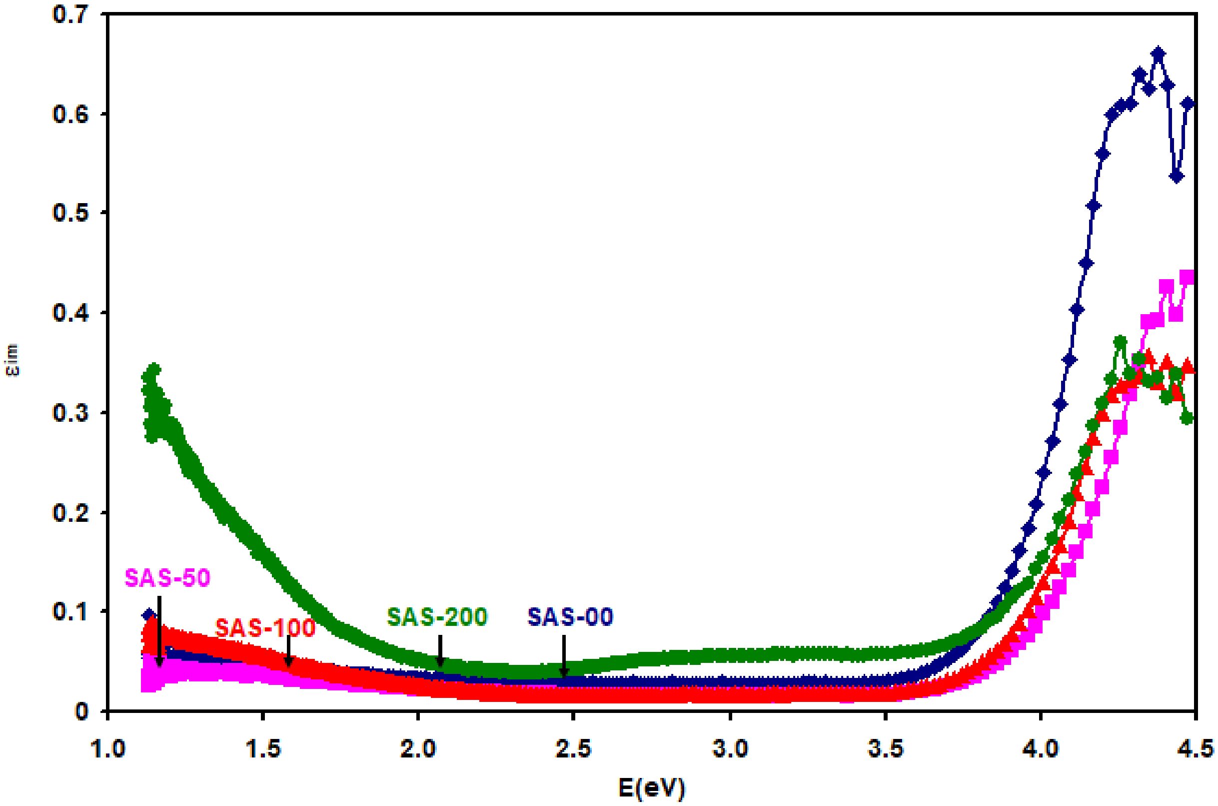

The imaginary part of the dielectric spectra.

Chapter Five

Conclusion

This thesis focused on enhancing transparent substrates so that they become adequate for optoelectronic applications. The target was reached by using SiO_2 as transparent substrates and sandwiching them with Au nanosheets to enhance their optical conductivities without losing their optical transparency. SiO_2 films of a thickness of 100 nm were prepared by the ion sputtering technique in two steps. The first was by depositing a 50 nm thick layer followed by a second layer of the same characteristics. Four types of samples were prepared and studied. They differ by varying the thickness of the Au nanosheets in the films. While structural analyses did not show a significant effect of Au nanosheets of the SiO_2 amorphous nature, a remarkable effect on the optical properties was observed. Optically, the thicker Au nanosheets lead to less transparency but high reflectivity and high dielectric constant values. The most significant effect is observed for the optical conductivity and its related parameters. Namely, with increasing Au layer thickness, the free charge carrier concentration increased by more than two orders of magnitude without remarkable decreases in drift mobility. In addition, the high-frequency dielectric constant increased from 2.55 to 3.2 and reached 11.0 as the Au layer thickness increased from 00 nm to 100 nm and reached 200 nm, respectively. The enhanced optical conductivity and its related parameters upon insertion of Au nanosheets between layers of SiO_2 are promising as they nominate the substrates under study for optoelectronic application.

References

Qiu, T., Akinoglu, E. M., Luo, B., Konarova, M., Yun, J. H., Gentle, I. R., & Wang, L. (2022). Nanosphere lithography: A versatile approach to develop transparent conductive films for optoelectronic applications. Advanced Materials, 34(19), 2103842.

Chinnasamy, S., & Ramanathan, S. (2020). Ruthenium (II) dicarboxylated bipyridyl based metal organic polymer as a sensitizer for nanostructured TiO2 based dye-sensitized solar cells (DSSC). Journal of Ceramic Processing Research, 21(1), 123-130.

Sangavi, T., & Ponpandian, N. (2024). Recent Developments in Solar Cells using Semiconducting Fibers. Semiconducting Fibers, 163-176.

Paramanik, B., Samanta, S., & Das, D. (2022). Near room-temperature synthesis of transparent conducting fluorine-doped ZnO thin films as window layer for solar cells. Optical Materials, 133, 112961.

Ou, S., Wang, J., Zhao, Y. A., Liu, X., Mo, Z., Wang, K., & Tao, C. (2023). Comparative study of liquid crystal variable retarder with rubbed polyimide and SiO2 thin films by glancing angle deposition. Modern Physics Letters B, 37(13), 2350016.

Liu, H., Wang, L., Jiang, Y., Li, S., Liu, D., Ji, Y., ... & Chen, D. (2018). Study on SiO2 thin film modified by post hot isostatic pressing. Vacuum, 148, 258-264.

Qasrawi, A. F., & Hamarsheh, A. A. (2021). Au/CdBr2/SiO2/Au Straddling-Type Heterojunctions Designed as Microwave Multiband Pass Filters, Negative Capacitance Transistors, and Current Rectifiers. physica status solidi (a), 218(22), 2100327.

Mushtaq, S., Arockiaraj, M., Klavžar, S., Fiona, J. C., & Balasubramanian, K. (2022). Comment on Mostar indices of SiO 2 nanostructures and melem chain nanostructures. International Journal of Quantum Chemistry, 122(11), e26894.

Utomo, R. S. B., Sentanuhady, J., & Muflikhun, M. A. (2024). TiO2–SiO2 nanocomposite via a novel sol-gel method with the addition of an energy monitoring device: Synthesized, characterization and anti-bacterial applications. Ceramics International, 50(13), 23367-23378.

Hwa, J. Y., & Sung, A. Y. (2023). Study of Contact Lens Materials with SiO2 Nanoparticle Additives Using the Sol-Gel Method. J Korean Ophthalmic Opt Soc, 28(4), 319-323.

Azmi, N., Safitri, R., Mursal, M., Amsir, A., & Masrurah, Z. (2024). Analisis Struktur Kristal Silika (SiO2) dengan Metode Sol Gel sebagai Aplikasi TLD (Thermoluminescence Dosimeter):-. ARMADA: Jurnal Penelitian Multidisiplin, 2(6), 361-366.

Kadri, L., Abderrahmane, A., Bulai, G., Carlescu, A., Doroftei, C., Motrescu, I., ... & Adnane, M. (2023). optical and structural analysis of TiO2–SiO2 nanocomposite thin films fabricated via pulsed laser deposition technique. Nanomaterials, 13(10), 1632.

Siddiqui, S. (2024). Atomic Layer Deposited (ALD) SiO2 with HiK/Metal Gate Dielectric for High Voltage Analog and I/O Devices on Silicon and High Mobility Silicon Germanium (SiGe) Channels: Planar, FinFET and GAA Transistor Architecture.

Xia, X., Li, J. S., & Khan, M. I. Band alignment of sputtered and atomic layer deposited SiO.

Lee, T., & Oh, S. (2024). Improvement of Amorphous InGaZnO Thin-Film Transistor Reliability and Electrical Performance Using ALD SiO $ _ {\text {2}} $ Interfacial Layer on PECVD SiO $ _ {\text {2}} $ Gate Insulator. IEEE Transactions on Electron Devices.

Guo, C., & Kong, M. (2020). Fabrication of ultralow stress TiO2/SiO2 optical coatings by plasma ion-assisted deposition. Coatings, 10(8), 720.

Darghlou, S. J. (2021). Effect of vertical deposition angle on structural and optical properties of tantalum oxide nano layers deposited by electron gun evaporation. Chinese Journal of Physics, 74, 226-238.

Tajima, N., Murotani, H., & Matsudaira, T. (2024). Ultra-low Refractive Index SiO2 Optical Thin Film with High Mechanical Strength by Sputtering and Electron Beam Evaporation. e-Journal of Surface Science and Nanotechnology.

Amata, H., Fu, Q., & Heidrich, W. (2023, August). Additive diffractive optical elements fabrication by PECVP deposition of SiO2 and lift-off process. In Digital Optical Technologies 2023 (Vol. 12624, pp. 23-28). SPIE.

Stępniak, M., Owczarek, S., Szyszka, A., Wośko, M., & Paszkiewicz, R. (2023). Characterization of the parasitic masking layer formed during GaN SA-MOVPE using PECVD SiO2 masks. Applied Surface Science, 640, 158325.

Chang, C. Y., Chen, H. C., Chang, C. H., Chen, K. H., Cai, C. E., & Wang, W. X. (2022, December). Stress analysis by finite element method stress for (ZrO2/SiO2) 2 anti-reflector multi-layer deposited with ion-assisted electron-gun evaporation. In Optical Technology and Measurement for Industrial Applications Conference 2022 (Vol. 12480, pp. 58-61). SPIE.

Zhang, Y., Shi, L., Geng, Z., Ren, T., & Yang, Z. (2019). The improvement of photocatalysis O2 production over BiVO4 with amorphous FeOOH shell modification. Scientific Reports, 9(1), 19090.

Das, R. C. (2021). The Effect of Stoichiometric Variation on the Magnetocaloric Properties of Selected Mn-Fe-Ni-Si-Al Intermetallic Compounds (Master's thesis, Miami University).

Kittel, C. (2021). Introduction to solid state physics Eighth edition.

Fox, M. (2002). Optical properties of solids. New York: Oxford University Press.

Trelles, M. A., & Calderhead, R. G. (2005). PHOTOTHERAPY UNVEILED: A REVIEW OF THE PHOTOBIOLOGICAL BASICS BEHIND ATHERMAL PHOTOBIOMODULATION WITH LASERS AND OTHER LIGHT SOURCES. PART 1: LIGHT-ITS PROPERTIES AND PARAMETERS. Laser therapy, 14(2), 87-95.

Pankove, J. I. (1975). Optical processes in semiconductors. Courier Corporation.

ISHAK, N. S., Che Seman, F., Yee, S. K., Zainal, N., Awang, N. A., & Zulkefli, N. U. H. H. Terahertz Spectroscopy Detection Combined with Frequency Selective Surface (Fss) on Fructose Solutions. SK and Zainal, NurFarina and Awang, Noor Azura and Zulkefli, Noor Ummi Hazirah Hani, Terahertz Spectroscopy Detection Combined with Frequency Selective Surface (Fss) on Fructose Solutions.

Amoah, P. K. (2024). Broadband Dielectric Spectroscopic Detection of Volatile Organic Compounds With Zinc Oxide and Metal-Organic Frameworks as Solid-State Sensor Materials.

Ramesh, P., Saravanan, K., Manogar, P., Johnson, J., Vinoth, E., & Mayakannan, M. (2021). Green synthesis and characterization of biocompatible zinc oxide nanoparticles and evaluation of its antibacterial potential. Sensing and Bio-Sensing Research, 31, 100399.

Vuong, P. (2018). Optical spectroscopy of boron nitride heterostructures (Doctoral dissertation, Université Montpellier).

Khusayfan, Najla M., and Hazem K. Khanfar. "Design and performance of (Au, Yb)/ZnS/InSe/C heterojunctions as plasmon resonators, photodetectors and microwave cavities." Journal of Electronic Materials 46.3 (2017): 1650-1657.

Zheng, X., Dong, M., Li, Q., Liu, Y., Di, X., Lu, X., ... & Li, Z. (2024). High-Performance UV Photodetector via Energy Band Engineering and LSPR-Enhanced Pyro-Phototronic Effect in Au Decorated 2D-PbI2/1D-ZnO Heterojunction. Advanced Optical Materials, 2303177.

Danylchuk, S. P., Zamurueva, O. V., Sakhnyuk, V. E., & Fedosov, S. A. (2021). Photonic properties of devices based on multicomponent crystalline compounds with content (Si, Ge, Sn). *Physics and Chemistry of Solid State*, *22*(3), 470-476.

Dijkstra, A. (2021). Optical properties of direct band gap group IV semiconductors.

Sreedevi, P. D., Vidya, R., & Ravindran, P. (2019). Earth-abundant nontoxic direct band gap semiconductors for photovoltaic applications by ab-initio simulations. Solar Energy, 190, 350-360.

Yuan, L. D., Deng, H. X., Li, S. S., Wei, S. H., & Luo, J. W. (2018). Unified theory of direct or indirect band-gap nature of conventional semiconductors. Physical Review B, 98(24), 245203.

Alharbi, S. R., Qasrawi, A. F., & Algarni, S. E. (2021). Effects of Ag2O nanosheets on the structural, optical, and dielectric properties of GeO2 stacked layers. physica status solidi (b), 258(5), 2000578.

Dresselhaus, M., Dresselhaus, G., Cronin, S. B., & Souza Filho, A. G. (2018). Solid State Properties. Alemania: Springer-Verlag.

Mohan, S., Kato, E., Drennen III, J. K., & Anderson, C. A. (2019). Refractive index measurement of pharmaceutical solids: a review of measurement methods and pharmaceutical applications. Journal of pharmaceutical sciences, 108(11), 3478-3495.

Soussi, A., Haounati, R., Ait hssi, A., Taoufiq, M., Asbayou, A., Elfanaoui, A., ... & Ihlal, A. (2023). First Principle Study of Structural, Electronic, Optical Properties of Co-Doped ZnO. Journal of Composites Science, 7(12), 511.

Hammou, B. A., El Oujdi, A., Echchelh, A., Dlimi, S., Liang, C. T., & Hemine, J. (2021). Modeling the bulk and nanometric dielectric functions of Au and Ag.

Qasrawi, A., Alharbi, S., & KJhusayfan, N. (2020). Thickness and annealing effects on the structural and optical conductivity parameters of zinc phthalocyanine thin films.

Axelevitch, A. (2021). Hot-probe characterization of transparent conductive thin films. Materials, 14(5), 1186.

Qasrawi, A. F., & Zyoud, H. M. (2020). Optical dynamics at the Au/ZnPc interfaces. Materials Research, 23(3), e20200064.

Kalachyova, Y., Alkhimova, D., Kostejn, M., Machac, P., Svorcik, V., & Lyutakov, O. (2015). Plasmooptoelectronic tuning of optical properties and SERS response of ordered silver grating by free carrier generation. RSC advances, 5(113), 92869-92877.

Yamada, A., & Yabana, K. (2024). Interaction of intense ultrashort laser pulses with solid targets: A systematic analysis using first-principles calculations. Physical Review B, 109(24), 245130.

Ezzeldien, M., Alrowaili, Z. A., & Hasaneen, M. F. (2021). Synthesis of an optimized ZnS/Au/ZnS multilayer films for solar cell electrode applications. Optical Materials, 113, 110814.

Udomsamuthirun, P., Changjan, A., Sukhonthachat, J., & Meesubthong, C. (2022). Effect of the plasmon mechanism on s-wave superconductors under high pressure in the weak-coupling limit. Physica C: Superconductivity and its Applications, 600, 1354104.

Xin, Y., Zhou, H., Ni, X., Pan, Y., Zhang, X., Zheng, J., ... & Jin, P. (2015). The optical properties of low infrared transmittance WO 3− x nanocrystal thin films prepared by DC magnetron sputtering under different oxygen ratios. RSC Advances, 5(71), 57757-57763.

Rao, M. G., Ramanjaneyulu, N., Pydi, B., Soma, U., Babu, K. R., & Prasad, S. H. (2023). Enhancing performance of dual-gate FinFET with high-K gate dielectric materials in 5 nm technology: a simulation study. Transactions on Electrical and Electronic Materials, 24(6), 557-569.

Haggren, T., Anttu, N., Mäntynen, H., Tossi, C., Kim, M., Khayrudinov, V., & Lipsanen, H. (2020). Management of light and scattering in InP NWs by dielectric polymer shell. Nanotechnology, 31(38), 384003.

Qu, Z., Yao, L., Ma, S., Li, J., He, J., Mi, J., ... & Feng, L. (2019). Rational design of HSNs/VO2 bilayer coatings with optimized optical performances and mechanical robustness for smart windows. Solar Energy Materials and Solar Cells, 200, 109920.

Al-Kuhaili, M. F. (2023). Transparent-conductive and infrared-shielding WO3/Ag/WO3 multilayer heterostructures. Solar Energy, 250, 209-219.

Sani, S. F., & Sendur, K. (2024). Thermal management of tungsten by spectrally selective thin film optical filters under laser illumination. International Journal of Thermal Sciences, 196, 108734.

Maeshima, H., Matsumoto, K., Hirahara, Y., Nakagawa, T., Koga, R., Hanamura, Y., ... & Ishikawa, D. (2022). Infrared absorption and its sources of CdZnTe at cryogenic temperature. Journal of Electronic Materials, 51(2), 564-576.

González Cuadra, J. (2023). Development of transparent semiconductor oxides with optical properties for the functionalization of glass surfaces.

Kamel, A. N., Pu, M., & Yvind, K. (2023). Surface defect effects in AlGaAs-on-Insulator photonic waveguides. Optics Express, 31(12), 20424-20439.

Kayani, Z. N., Anjum, M., Riaz, S., Naseem, S., & Zeeshan, T. (2020). Role of Mn in biological, optical, and magnetic properties ZnO nano-particles. Applied Physics A, 126, 1-17.

Ullah, A., Khan, M. I., Almutairi, B. S., Laref, A., & Dahshan, A. (2024). Trans-polyacetylene doped Cs2AgBiBr6: Band gap reduction for high-efficiency lead-free double perovskite solar cells. Results in Physics, 107654.

Cahyo, I. N., Aini, N., Steky, F. V., Suendo, V., Safitri, W. N., & Prasetyo, A. (2023). Synthesis of plate-like Fe-doped SrBi4Ti4O15 using Na2SO4/K2SO4 molten salt method: XRD, Raman spectroscopy, SEM, and UV–VIS DRS studies. Journal of the Iranian Chemical Society, 20(12), 3079-3085.

Bhatia, S., Verma, N., & Aggarwal, M. (2018). Effect of deposition time on sputtered ZnO thin films and their gas sensing application. Journal of Materials Science: Materials in Electronics, 29(21), 18136-18143.

Bačík, P., & Fridrichová, J. (2019). The site occupancy assessment in beryl based on bond-length constraints. Minerals, 9(10), 641.

Kitaura, M., Nakagawa, H., & Ohnishi, A. (2002). Optical spectra and electronic structures of forsterite (α-Mg2SiO4) single crystals. Journal of the Physical Society of Japan, 71(11), 2736-2741.

Riungu, G. G., Mugo, S. W., Ngaruiya, J. M., John, G. M., & Mugambi, N. (2021). Optical band energy, Urbach energy and associated band tails of nano crystalline TiO2 films at different annealing rates. American Journal of Nanosciences, 7(1), 28-34.

Mojica, R., Torres, A. E., Zumeta-Dubé, I., Avila, Y., & Reguera, E. (2022). Optical bandgap of Cd, Zn, and Ag nitroprussides. A combined experimental and computational study. Journal of Physics and Chemistry of Solids, 163, 110608.

Debnath, D., Halder, P., Saha, B., Acharya, H., & Ghosh, S. K. (2024). Fermi–Dirac statistics in correlation between electronic entropy and spatial confinement of liquid crystal-perovskite nanohybrids. Journal of Materials Chemistry C.

Khalil, M. I., Saad-Bin-Alam, M., & Rahman, A. (2013, December). Resolution limit of subwavelength optical imaging through Au-SiO 2-Au nanorod arrays. In 2013 2nd International Conference on Advances in Electrical Engineering (ICAEE) (pp. 129-131). IEEE.

Chanana, R. K. (2019). Interrelated current-voltage/capacitance-voltage traces based characterisation study on 4H-SiC metal-oxidesemiconductor devices in accumul ation and Si device in inversion along with derivation of the average oxide fields for carrier tunnelling from the cathode and the anode. IOSR-JEEE, 14(3), 49-63.

Qasrawi, A. F. (2019). Effect of Y, Au and YAu nanosandwiching on the structural, optical and dielectric properties of ZnSe thin films..

ملخص الرسالة

وفي هذه الاطروحة ، صنعت مواد تحتية موصلة شفافة تُستخدم في صنع الأجهزة الإلكترونية الموصلة . وتتكون هذه الطبقة من طبقتين من SiO_2 مسندتين بصفائح نانوية من Au مختلفة السمك 50 نانومتر، و100 نانومتر، و200 نانومتر لتشكيل ثلاثيات SiO_2/Au / SiO_2 (SAS-xx). وتُخضع هذه الطبقات لتحليل هيكلي وبصري لاستكشاف التعديلات الفيزيائية المحتملة التي يمكن أن تنتج عن مشاركةAu في طبقة أو في بنية SiO_2. ومن الملاحظ أن الصفائح النانوية من الذهب لم تغير الطابع غير المتبلور لهيكل SiO_2 ولكنها عززت خصائصه البصرية والكهربائية إلى حد كبير. ويلاحظ على وجه الخصوص أن عينات SAS-00 التي لا تحتوي على AU تظهر شفافية عالية وانعكاسات منخفضة. الطبقة الاسمك من صفيحة الذهب ,الاقل في الشفافية والاعلى في الانعكاس. ونتج عن طبقات الذهب أيضاً انخفاض في استيعاب SiO_2 للضوء. غير أن صفيحة الذهب النانوية عززت استيعاب الناقل الحر في نطاق الضوء دون الأحمر وقللت الفجوة الفاصلة بين نطاقات الطاقة في SiO_2 . عينات SAS التي لا تتألف من أي طبقة من الذهب ، أو صفيحة نانوية من سمك 50 نانومتر تظهر خصائص شبه الموصلات غير المتحللة وتبين وجود حالات ذيل الطاقة في الفجوة الفاصلة. وقد اختفت هذه الذيول مع زيادة سمك طبقة الذهب. ويلاحظ أيضاً أن الصفائح النانوية الخاصة بالذهب تحسن قيمة الكهرباء والاستجابة. وأظهرت عينات SAS-200 وجود خاصية مواد كهربية ذات high-k gate مع قيمة كهربية تتجاوز ال 40. وبالإضافة إلى ذلك، يلاحظ أن الصفائح النانوية من الذهب زادت من القدرة البصرية على التوصيل وكثافة الشحنات الحرة في السيليكون دايوكسايد، مما جعلها ذات قدرة عالية على التوصيل. وتشير هذه الخواص بأنه قد تستخدم كأقطاب كهربائية ذات high- k gate وتدخل في تصميم الأجهزة الإلكترونية البصرية.